J. Phase Equilib. Diffus. (2021) 42:748–771
https://doi.org/10.1007/s11669-021-00913-w

SUPPLEMENTAL LITERATURE REVIEW

Additive Manufacturing of High-Entropy Alloys: Microstructural Metastability and Mechanical Behavior

Shuai Guan[1] · Jie Ren[1] · Shahryar Mooraj[1] · Yanfang Liu[1] · Shuai Feng[1] · Shengbiao Zhang[1] · Jian Liu[1] · Xuesong Fan[2] · Peter K. Liaw[2] · Wen Chen[1]

Submitted: 26 April 2021 / in revised form: 29 May 2021 / Accepted: 22 June 2021 / Published online: 9 August 2021

Abstract High-entropy alloys (HEAs) have received considerable interest over the past decade due to their intriguing structural, chemical, and physical properties. Additive manufacturing (AM), also termed three-dimensional (3D) printing, generates parts with complex geometries and internal features layer-upon-layer from a computer-aided design (CAD) 3D file. In recent years, explosive research on AM of HEAs has been inspired. This paper performs a comprehensive and critical review on the recent progress in additively manufactured (AM-ed) HEAs, with a special focus placed on the similarities and differences in the microstructure and mechanical behavior between the AM-ed HEAs and the as-cast or thermo-mechanically processed (TMP-ed) counterparts. To gain a better understanding of the formation of the AM microstructure, the working principles, rapid solidification effects, and subsequent thermal cycling effects of various metal AM techniques, e.g., directed energy deposition (DED), selective laser melting (SLM), and electron beam melting (EBM), are also introduced. In the end, several future research directions are suggested towards the design of advanced HEAs with the superior strength-ductility synergy via 3D printing.

Keywords additive manufacturing · high-entropy alloys · mechanical behavior · microstructural metastability · rapid solidification · thermal cycling

1 Introduction

The conventional alloy-design approach often produces alloys based on a single host element (e.g., Fe in steels), with modifications by small amounts of alloying elements (e.g., C in steels) to tailor the material properties. In contrast, a recent decade has witnessed an emerging-paradigm shift from conventional alloys to so-called high-entropy alloys (HEAs), which comprise multi-principal elements that are mixed equiatomically or near-equiatomically.[1–3] Such a compositional characteristic often leads to an increased configurational entropy and hence, the formation of multi-component solid solutions. Typically, HEAs crystallize as a single-phase face-centered-cubic (FCC), body-centered-cubic (BCC), or hexagonal-close-packed (HCP) solid-solution structure.[4–10] Several HEAs with multi-phase (e.g., FCC plus BCC) microstructures have also been designed.[11–13] Since their emergence, HEAs have aroused considerable research interest due to their extraordinary mechanical properties,[4, 14] paired with superior corrosion and irradiation resistance.[6,15,16] To date, HEAs are often processed by conventional routes, such as casting,[4,5,17, 18] powder metallurgy,[19, 20] and magnetron co-sputtering.[21] A post treatment, such as thermomechanical processing (TMP), is often required to refine the as-cast microstructure towards desired

This article is part of a special topical focus in the *Journal of Phase Equilibria and Diffusion* on the Thermodynamics and Kinetics of High-Entropy Alloys. This issue was organized by Dr. Michael Gao, National Energy Technology Laboratory; Dr. Ursula Kattner, NIST; Prof. Raymundo Arroyave, Texas A&M University; and the late Dr. John Morral, The Ohio State University.

✉ Wen Chen
wenchen@umass.edu

[1] Department of Mechanical and Industrial Engineering, University of Massachusetts, Amherst, MA 01003-2210

[2] Department of Materials Science and Engineering, The University of Tennessee, Knoxville, TN 37996

properties.[4,17] As-for magnetron co-sputtering, it is often used to manufacture thin films for ultra-small-dimension devices.[21] Furthermore, these conventional metallurgical processes are often used to generate simple-geometry parts. In contrast, additive manufacturing (AM), also termed three-dimensional (3D) printing, produces parts directly from a 3D digital model via a layer-by-layer route, enabling the build-up of large-scale parts with complex geometries and internal features. In addition, the AM process is often characterized by a highly-localized melting and solidification process that leads to the formation of extremely non-equilibrium microstructures and thus, unusual mechanical properties.[22] Several commercial alloys, such as 316L stainless steel,[22,23] Al-Si alloys,[24] and Inconel superalloys,[25] have been successfully printed, and recently 3D printing of HEAs has also received explosive research interest.[26]

This paper aims to perform a comprehensive review on the microstructures and mechanical behavior of additively manufactured (AM-ed) HEAs. In particular, the similarities and differences in the microstructures and mechanical behavior of the AM-ed HEAs versus conventionally processed counterparts are discussed. To gain a fundamental understanding of the microstructure formation of HEAs during AM, the working principles, rapid solidification, and thermal cycling effects of various metal AM techniques are reviewed. Finally, we suggest some future research directions towards advanced HEAs with an exceptional strength-ductility synergy via 3D printing.

2 Metal Additive Manufacturing

2.1 Working Principles

Several metal AM approaches, including directed energy deposition (DED), selective laser melting (SLM), electron beam melting (EBM), and direct ink writing (DIW), have been used to produce HEAs. DED is a laser powder-blown AM process, during which the metal particles are blown from a powder hopper and injected into a melt pool created by a high-energy laser beam, as shown in Fig. 1(a).[27] The substrate moves in the *x*-*y* plane following a pre-defined path, and hence a moving melt pool is created until a cross-sectional layer of the designed part is complete. Then the deposition head moves up in the *z* direction to build consecutive layers. It should be pointed out that via DED, functional coatings can be produced and damaged components can be repaired.[28] Moreover, compositional heterogeneity can be achieved spatially within a single DED part if different types of particles are loaded in separate powder hoppers and fed simultaneously.[29] In contrast, SLM and EBM are powder-bed fusion AM processes instead of powder-blown ones, as shown in Fig. 1(b) and (c).[30, 31] SLM works with a high-energy laser beam, whereas EBM works with a high-energy electron beam. During powder-bed fusion AM processes (i.e., SLM and EBM), a thin layer (several tens of μm) of metal particles is spread onto a powder bed and then melted selectively according to a pre-defined path. Then the build platform moves downwards (in the *z* direction) by the pre-defined layer thickness, and the subsequent layers are deposited until the completion of the designed part. In general, DED, SLM, and EBM are energy-intensive AM approaches that are characterized by rapid solidification and subsequent heating-cooling thermal cycles. Such a complex thermal history produces extremely non-equilibrium microstructures, which are not readily accessible via conventional metallurgical routes. In contrast, in the DIW AM process, a colloidal particle suspension ink is dispensed out of a micro-nozzle and deposited along a pre-defined path (see Fig. 1d).[32] The printed green parts are subsequently sintered and consolidated via the post heat treatments,[32, 33] thereby allowing for significant mitigation of rapid-solidification-induced thermal residual stresses as in other AM processes.

2.2 Rapid Solidification and Thermal Cycling

As aforementioned, DED, SLM, and EBM are energy-intensive AM approaches that involve rapid heating and melting of metallic powders, followed by rapid solidification. Deposition of subsequent layers induces heating-cooling thermal cycles on the as-solidified layers, as presented in Fig. 2.[34] It is of critical importance to understand the complex thermal process, as it significantly affects the microstructures and hence, mechanical properties of the AM-ed materials. The rapid solidification of the melt pool is characteristic of large temperature gradients and fast cooling rates. The temperature gradient and cooling rate can be calculated from the temperature field that is often quantified by experimental or numerical approaches. The temperature field can be measured by thermocouples[34] or thermal imaging pyrometers.[34–37] For example, the temperature variations at a specific location of the built part can be recorded by the thermocouple throughout the printing process. In other words, the heating-cooling profile at a specified location can be recorded in real time. In contrast, the high-speed thermal imaging pyrometer is often used to measure the temperature field of the melt pool surface.[38–40] Besides these measurement methods, numerical approaches have been developed to simulate the temperature field and hence, the temperature evolution during printing.[35,37, 41–44] As for the numerical approaches, the heat-source characteristics, the heat-source-metal particle interaction, and the heat-

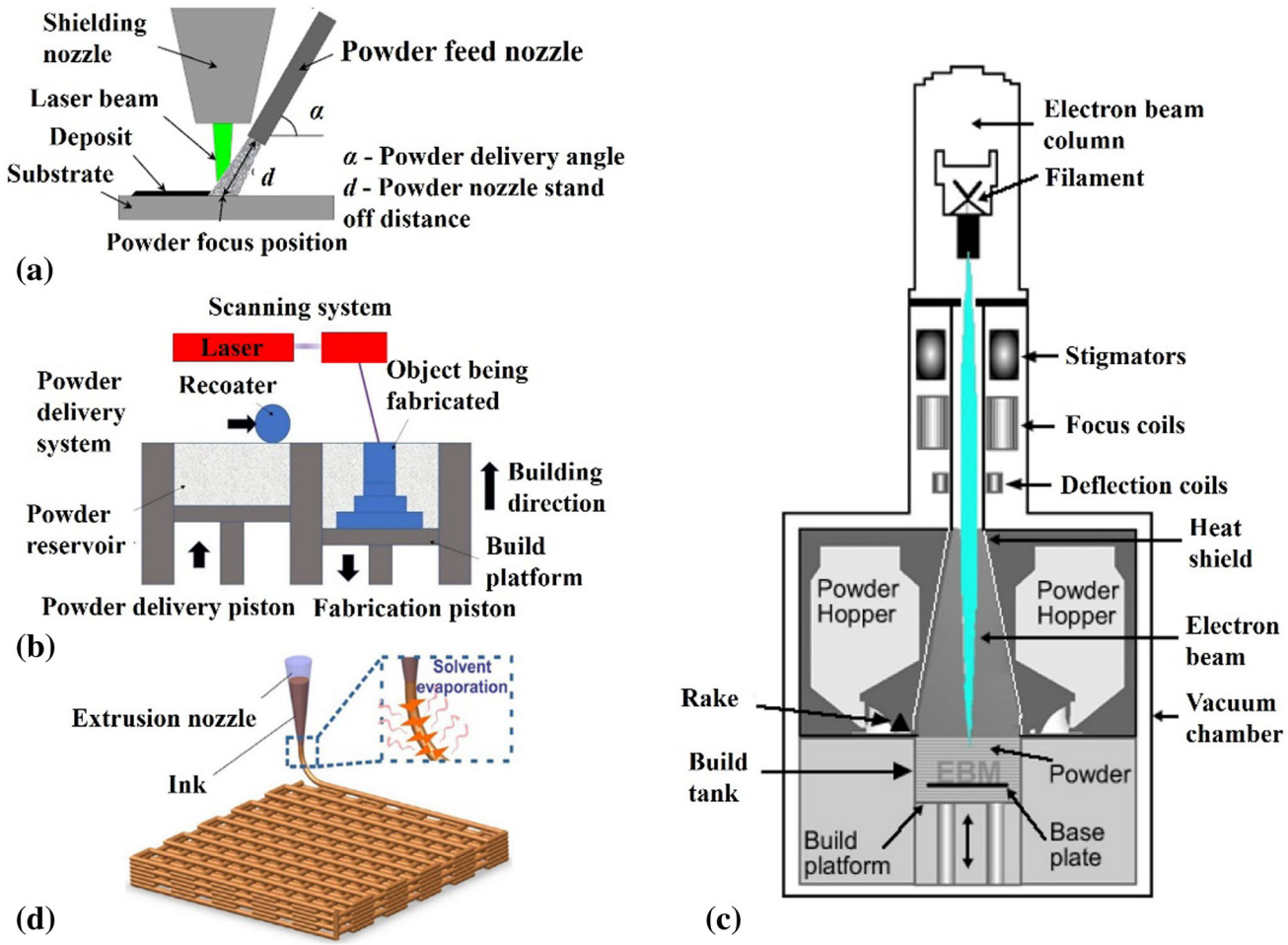

Fig. 1. Schematics for (a) DED, (b) SLM, (c) EBM, and (d) DIW processes. (a) Reproduced with permission.[27] (b) Reproduced with permission.[30] (c) Reproduced with permission.[31] (d) Reproduced with permission[32]

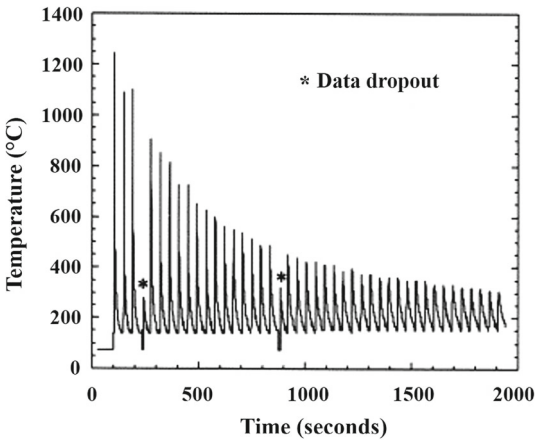

Fig. 2. Temperature profile of the first layer of the H13 tool steel during the deposition of subsequent 20 layers. Reproduced with permission from Ref 34

transfer process need to be carefully considered. The heat source often follows an axisymmetric Gaussian profile:[45]

$$P_{\mathrm{d}} = \frac{fP}{\pi r_b^2}\exp\left(-f\frac{r^2}{r_b^2}\right) \quad \text{(Eq 1)}$$

where P_{d} is the power density, r_b the heat source radius, P the total power of the heat source, f the distribution factor, and r the radial distance of any point from the axis of the heat source. As for the heat source-metal particle interaction, it should be noted that the heat energy cannot be fully absorbed by the deposit, and a portion of energy is wasted. For example, for the powder-bed AM processes, the total incident energy has to be reflected several times and only a portion of the total energy is eventually absorbed by the powder bed. Therefore, the particle's absorptivity should be reasonably considered.

The melt pool cools down and solidifies via multiple heat-transfer mechanisms, i.e., conduction, convection, and radiation. Several models have been proposed to simulate the heat-transfer process. However, over-simplifications would lead to a decreased computational accuracy. For example, in the Eagar–Tsai model, the temperature

dependence of the thermo-physical parameters (i.e., specific heat capacity, density, and thermal conductivity), and the possible phase transformation are not taken into account, which significantly decreases the predictive accuracy.[46,47] In a study by Johnson et al.,[47] both phase transformations and phase-dependent thermo-physical parameters are taken into account, which reaches a good compromise between computational accuracy and efficiency. Besides those experimental and numerical methods, the cooling rate during melt-pool solidification can also be roughly estimated from the measured solidification structure scale according to well-established empirical relations.[48]

The temperature gradient and cooling rate during AM are closely related to the specific printing parameters. Table 1 gives a summary of the printing parameters for some typical HEAs. During DED, the scan speed is as low as a dozen mm/s, and hence, the linear heat input (i.e., ratio of the laser power to scan speed) can be as high as tens to hundreds of J/mm. Consequently, the layer-thickness and hatch-spacing values are often large (150-500 μm). During SLM, the scan speed can reach up to several thousands of mm/s, and thus, the linear heat input is as low as 0.1-0.5 J/mm. Accordingly, the layer-thickness and hatch-spacing values are significantly smaller (25-110 μm). Such distinct printing parameters between DED and SLM are responsible for the differences in the temperature gradient and cooling rate. Typically, the temperature gradient and cooling rate during DED are 10^2-10^3 K/mm and 10^3-10^4 K/s, respectively,[35, 37, 41, 49–51] as compared to those of 10^3-10^5 K/mm and 10^4-10^7 K/s, respectively during SLM.[48, 52–54]

2.3 Microstructure Formation

The large temperature gradient (G) during melt-pool solidification facilitates the formation of columnar microstructures, with crystallographic textures.[48, 55, 56] The crystallographic textures often lead to anisotropic mechanical properties,[57, 58] and extensive attempts have been made to achieve the fine and equiaxed microstructures, with decreased crystallographic textures. The solidification grain geometry is collectively controlled by the temperature gradient (G) ahead of the solidification interface and solidification front growth velocity (V). Equiaxed grains tend to form in the region nearby the melt-pool surface where low G and high V values prevail.[50, 55, 56, 59–69] However, these equiaxed grains located nearby the melt pool surface may be partially or even completely erased due to the subsequent remelting process. Consequently, it is difficult to achieve fully-equiaxed microstructures in the AM-ed alloys.[70–72] Surprisingly, in a recent study by Guan et al.,[38] a six-component HEA $AlCoCrFeNiTi_{0.5}$ was reported to form equiaxed microstructures with random crystallographic textures. In their study, various laser powers and scan speeds were used, hence creating a wide range of G and V (see Fig. 3a). With no exception, a fully-equiaxed microstructure was achieved (see Fig. 3b). The formation of the equiaxed microstructure was well understood within the framework of Gäumann's model.[73] The Gäumann's model estimates

Table 1. Printing parameters used for some typical HEAs reported in literature

HEA system	AM method	Laser power, W	Scan speed, mm/s	Layer thickness, μm	Hatch spacing, μm	References
CoCrFeMnNi	DED	400	5	154	460	39
	SLM	160-290	1500-2500	40	50	81
$(CoCrFeMnNi)_{99}C_1$	SLM	90	200, 600	25	80	53
	SLM	90	200	25	80	138
CoCrFeNi	SLM	150	270	50	100	96
$CoCrFeNiC_{0.05}$	SLM	200-400	400-3000	50	110	98]
	SLM	400	800	…	…	119
$CoCrFeNiAl_{0.3}$	DED	300	17	254	381	126
$Ni_{2.1}CoCrFeNb_{0.2}$	DED	1600	7	300	…	127
Mo-Nb-Ta-W systems	DED	800	4.2	~ 508	…	51
$AlCo_xCr_{1-x}FeNi$	DED	200-300	6.7	250	…	103
$CoCrFeNiAl_x$ (x = 0.3-0.7)	DED	300	6.7	…	…	134
$(CoCrFeMnNi)_{100-x}Al_x$ (x = 0, 2, 5, 8)	DED	1400	10	…	…	125
$Al_{0.5}CrMoNb$	EBM	…	80	50	…	139

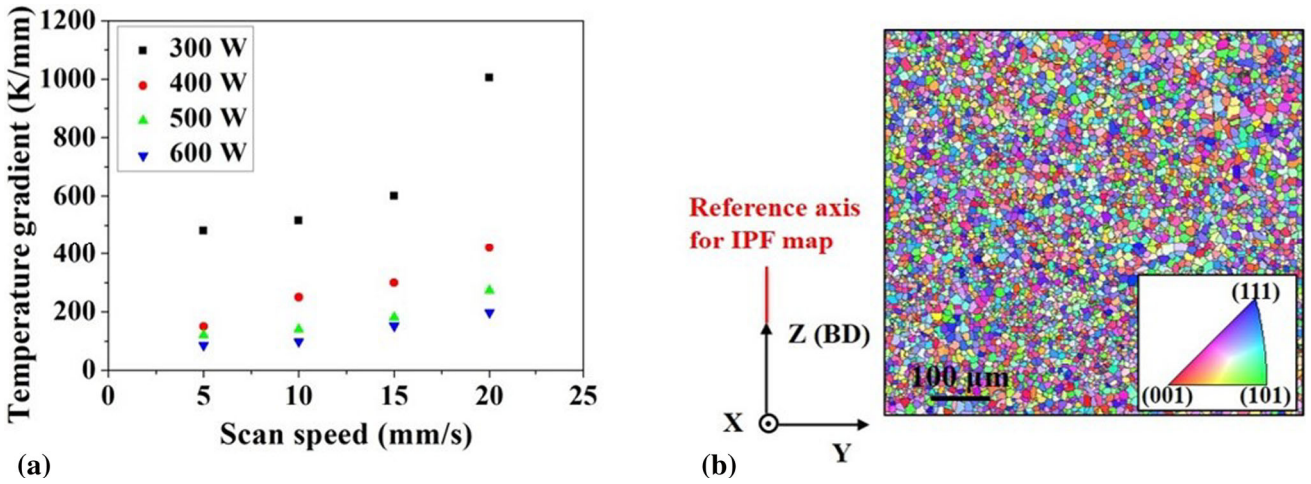

Fig. 3. Printing of the $AlCoCrFeNiTi_{0.5}$ HEA via DED. (a) Temperature gradients as a function of laser powers and scan speeds. (b) Electron back-scattered diffraction (EBSD) inverse pole figure (IPF) map, showing a fully-equiaxed microstructure. (a)–(b). Reproduced with permission from Ref 38

the volume fraction, ϕ, of the equiaxed crystals at the solidification front, and as proposed by Hunt,[74] when the ϕ value reaches or exceeds 49%, the equiaxed growth will dominate over the columnar growth, and a fully-equiaxed microstructure can be achieved. The parameters used in Gäumann's model was largely estimated by Thermo-Calc. Based on this approach, the ϕ values corresponding to various *G*–*V* combinations were calculated to be greater than 49%, thus providing theoretical basis for the observed equiaxed microstructures.

The equiaxed microstructure can also be achieved with the assistance of external stimuli, a well-established wisdom as demonstrated in traditional casting[75, 76] and welding[77] literature. For example, in a study by Zuo et al.,[75] the intensive melt shearing was shown to promote the formation of fine and equiaxed microstructures in the as-cast Mg alloys. In another study by Yuan et al.,[77] the arc oscillation was shown to facilitate the microstructure transformation from the columnar to equiaxed grain in Mg alloys during welding. As such, it can be envisioned that the grain structure formed during 3D printing can also be influenced by the external forces, and such an idea has been recently proven. In a study by Todaro et al.,[78] IN625 superalloy specimens were printed with the assistance of an ultrasonic device. Surprisingly, a fine equiaxed γ microstructure with a random crystallographic texture was achieved (see Fig. 4b and d). For comparative purposes, a conventional microstructure with morphological and crystallographic textures is also shown (see Fig. 4a and c). Furthermore, the grain structure can be readily manipulated by periodically switching the ultrasonic device on and off (see Fig. 4e). Enhanced dendrite fragmentation is assumed to be responsible for the grain-structure evolution in the presence of external forces. The presence of those external forces promotes the dendrite fragmentation during solidification due to multiple effects, for example, remelting and mechanical breakup.[77] These fragments may serve as new equiaxed crystal embryos, promoting the formation of equiaxed microstructures. To the best of our knowledge, 3D printing of HEAs with the assistance of external forces has not been reported.

Aside from the rapid solidification, the in-situ thermal cycling during AM can cause significant microstructural evolution. For example, in a study by Fujieda et al.,[79] they printed an equiatomic HEA AlCoCrFeNi via EBM. Figure 5 gives the EBSD inverse pole figure (IPF)and phase maps of the top and the bottom parts of this EBM-ed AlCoCrFeNi HEA. Clearly, the grain structure, crystallographic texture, and phase content are different in both regions. The bottom region includes more equiaxed grains with random textures than the top region. Also, the bottom region contains more FCC phases, which are located at the grain boundaries of BCC phases, than the top region. Such microstructural heterogeneities along the build direction was ascribed to the microstructural evolution of the as-solidified region during 3D printing. The bottom region is exposed to a longer pre-heating duration than the top part that triggers the phase transformation from the BCC to FCC phase. In another study by Kürnsteiner et al.,[80] a Fe19Ni5Ti (weight percent) maraging steel was additively manufactured via DED. Often, a two-step phase transformation is needed to achieve the required properties, i.e., the austenite-to-martensite phase transformation and subsequent nanoscale NiTi precipitation in the martensite. Through the control of the heating-cooling thermal cycle, these two-phase transformations are in-situ activated during printing. In their study, this Fe19Ni5Ti maraging steel was not continuously printed, but with a 120-s pause after a

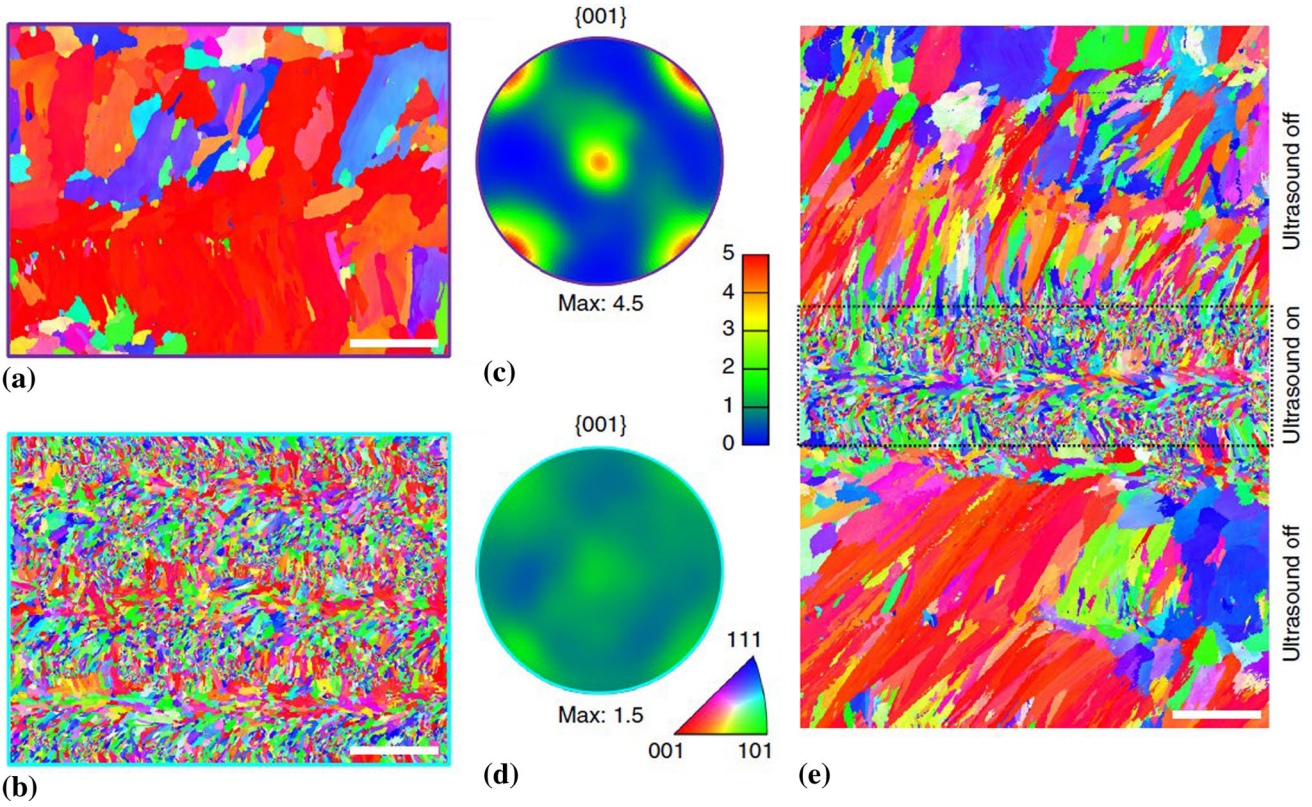

Fig. 4. AM of the IN625 superalloy without (a, c) and with (b, d) high-intensity ultrasonic vibration assistance. (e) Control of the grain structure by periodically switching the ultrasonic device on and off. Scale bars: 250 µm. (a)–(e). Reproduced with permission from Ref 78

Fig. 5. EBSD IPF maps (a) and phase maps (b) of the top and the bottom parts of the EBM-ed AlCoCrFeNi HEA. (a)–(b). Reproduced with permission from Ref 79

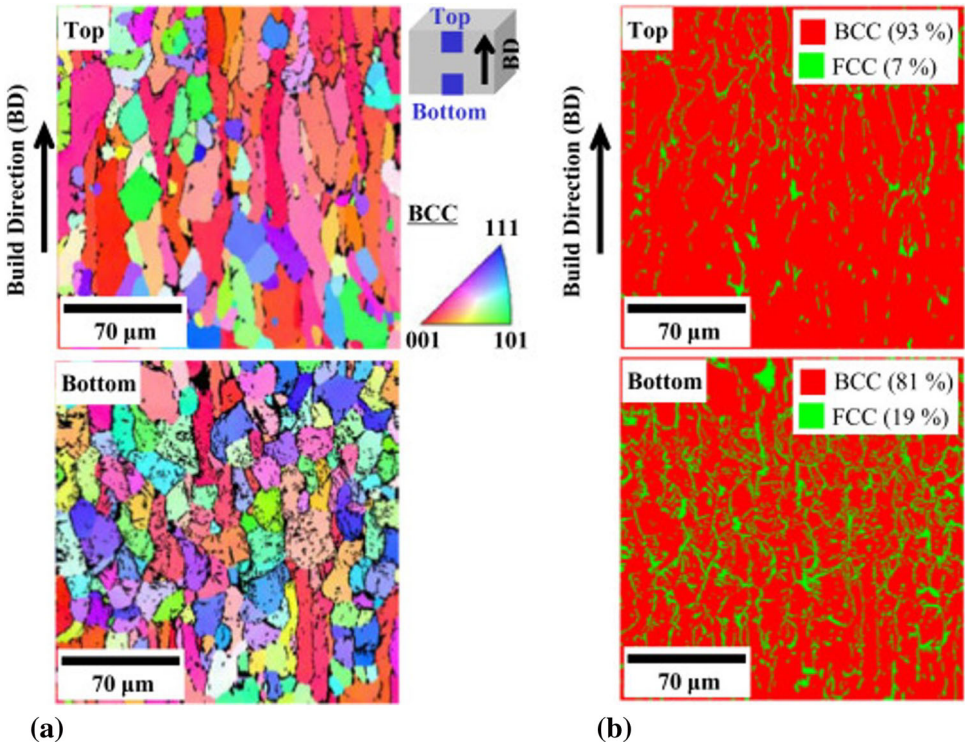

block of four layers. During this pause (i.e., the laser was switched off), the block was cooled down below the martensite-transformation temperature, M_s, with a dark layer introduced. Hence, a partial austenite-to-martensite transformation occurs, and some austenite phases at grain boundaries are retained. During subsequent deposition cycles, a series of temperature spikes are exposed, triggering the precipitation of the nanoscale η-NiTi phases in the martensite of the dark layer. Finally, a complex and hierarchical microstructure was achieved, leading to enhanced tensile properties.

3 Microstructures and Mechanical Behavior of AM-ed HEAs

To date, the AM process has been used to synthesize several HEA systems, including $AlCoCrFeNiTi_{0.5}$,[38] CrMnFeCoNi,[39, 81–91] $Al_xCoCrFeNi$,[72, 79, 92–98] $Co_{0.5}CrCu_{0.5}FeNi_{1.5}AlTi_{0.4}$,[99] TiZrNbMoV,[100] $Co_{1.5}CrFeNi_{1.5}Ti_{0.5}Mo_{0.1}$,[101] and AlCoFeNiSmTiVZr,[102] compositionally-graded HEAs,[103–106] and laminated HEAs,[40, 107] etc. The microstructures and mechanical properties of these AM-ed HEAs are reviewed in this section, and the microstructural features of some typical AM-ed HEAs are summarized in Table 2. In this section, we begin with FCC-based and BCC-based HEAs. Then we focus on certain HEAs with transformation induced plasticity (TRIP) effects during straining. Finally, we divert to compositionally-graded HEAs and finally to laminated HEAs.

3.1 FCC-Based HEAs

3.1.1 Single-Phase FCC HEAs

The equiatomic alloy, CoCrFeMnNi (so-called Cantor alloy), is a typical single-phase FCC HEA and receives the most attention for 3D printing due to its extraordinary mechanical properties.[4] In a study by Zhu et al.,[81] the SLM-ed CoCrFeMnNi was reported to show a hierarchical microstructure across multiple length scales, i.e., melt pools (tens of micrometers), columnar grains ($\sim$ 12.9 μm), and solidification cell structures ($\sim$ 0.34 μm) (see Fig. 6). Such a hierarchical microstructure has also been reported for a SLM-ed 316L stainless steel.[22] The columnar grains are common in AM-ed alloys due to the large thermal gradient inherent to AM. Furthermore, the cellular structures can be attributed to the constitutional undercooling and the fast-cooling rate that prohibits the formation of secondary and tertiary arms. The fast-cooling rate may also suppress the segregation kinetics and hence, lead to a uniform elemental distribution (see Fig. 6h). It can also be seen from Fig. 6 that a <100> crystallographic texture was formed along the build direction. This is because cubic alloys preferentially align one of their six <100> crystallographic directions along the maximum heat flux direction during solidification. Note that the as-deposited microstructure of CoCrFeMnNi is highly sensitive to the specific AM-processing protocol. For example, in a study by Piglione et al.,[83] the SLM-ed CoCrFeMnNi single-track single-layer build was also reported to show columnar grains (see Fig. 7a). However, these columnar grains grow along the direction perpendicular to the local melt pool boundary, forming a convergent pattern, and these columnar grains form a random crystallographic texture (Fig. 7a). Such a random crystallographic texture is totally different form the <100> crystallographic texture reported by Zhu et al.,[81] and can be well understood in view of the build-substrate interactions. The epitaxial growth from existing grains in the polycrystalline substrate inevitably results in a random crystallographic texture. In contrast, in the multi-track-/multi-layer builds, the number of grains within a single melt pool decreases substantially due to the promoted competitive grain growth. Furthermore, due to the competitive grain growth, a crystallographic texture can be finally achieved after a certain build height, i.e., <100> or <110> orientations parallel to the build direction (Fig. 7b). Similar crystallographic textures can also be found in other SLM-ed CoCrFeMnNi specimens.[108] In contrast, DED-printed CoCrFeMnNi HEAs show a more random crystallographic texture, as evidenced from Refs 39, 88.

Besides the crystallographic texture, the grain structure of CoCrFeMnNi can also be manipulated. For example, in a study by Li et al.,[109] a DED-ed CoCrFeMnNi HEA single-track build was reported to achieve a small portion of equiaxed grains at the very top of the melt pool. In another study by Zheng et al.,[110] they even achieved fully equiaxed microstructures in CoCrFeMnNi HEAs via the DED process. As shown in Fig. 8(a) and (b), a near fully-equiaxed microstructure was achieved at a laser scan speed of 3 mm/s, whereas the conventional columnar microstructure was achieved at a higher laser scan speed of 4 mm/s. A microstructure-selection map with three distinct regions, i.e., columnar, mixed, and equiaxed, was established in their study, showing that the decrease in the scan speed can result in a *G*–*R* combination (note they used *R* instead of *V* to denote solidification front velocity) that locates in the equiaxed domain. As such, the equiaxed microstructure with a random crystallographic texture can be formed instead of the columnar microstructure with a <110> crystallographic texture (see Fig. 8a and b). Furthermore, the equiaxed microstructure with a random crystallographic texture exhibits a more pronounced strain-hardening rate and hence, an enhanced ultimate tensile

Table 2. Summary of microstructural features of some typical HEAs printed via DED, SLM, or EBM

HEA system	AM method	Microstructural features	References
CoCrFeMnNi	SLM	Columnar grains; grain size of ~ 12.9 μm; <100> texture along build direction; cellular structures; dislocation cells (~ 0.34 μm); no elemental segregation observed	[81]
CoCrFeMnNi	DED	Columnar grains; grain size of ~ 13 μm; weak texture; cellular structures (2-5 μm); dense dislocations but not in the form of cells; Mn and Ni segregated at cellular walls, and Co, Cr, and Fe segregated at cellular interiors	[39]
CoCrFeMnNi	DED	Columnar grains; weak texture; cellular structures (3-4 μm); dense dislocations but not in the form of cells; Mn and Ni segregated at cellular walls, and Co, Cr, and Fe segregated at cellular interiors	[88]
CoCrFeMnNi	DED	Both columnar and equiaxed microstructures can be achieved via adjusting the printing parameters (scan speed); grain sizes of 30-46 μm; equiaxed microstructures show random crystallographic textures, whereas columnar microstructures present a strong <110> texture (along the build direction)	[83]
$(CoCrFeMnNi)_{99}C_1$	SLM	Columnar grains; grain size of 20-35 μm; cellular structures (180-330 nm); Mn-rich oxide and sulfide and Cr-rich carbide precipitates (1.13-1.73 volume-percent (vol.%); 20-80 nm) preferentially at cellular boundaries; dislocation density of 10^{14} m^{-2}	[53, 138]
CoCrFeMnNi reinforced with TiN	SLM	Nearly equiaxed grains; refined grain size down to a few micrometers; TiN nanoparticles preferentially segregate at grain boundaries	[120–122]
CoCrFeMnNi reinforced with TiC	DED	Columnar grains: TiC particles uniformly distributed	[124]
CoCrFeMnNi reinforced with WC	DED	Equiaxed grains; $Cr_{23}C_6$ precipitates at micrometer-scale along some ~ 100 nm cubic precipitates (unidentified)	[123]
$CoCrFeNiC_{0.05}$	SLM	Columnar grains; cellular structures (500-1,000 nm); a high density of dislocations; FCC single-phase microstructure, no $Cr_{23}Cr_6$ precipitates	[98]
$CoCrFeNiC_{0.05}$	SLM followed by 800 °C aging	As-deposited cellular structures (500-1000 nm) disappear after aging; in addition to the FCC matrix, $Cr_{23}Cr_6$ precipitates are formed preferentially at grain boundaries	[119]
$Al_{0.2}Co_{1.5}CrFeNi_{1.5}Ti_{0.3}$	SLM	Grain size of ~ 27 μm; cellular structures (~ 527 nm); segregation of Ti and Al at cellular walls; FCC matrix plus a dispersion of corundum particles (~ 5 nm); after ageing, spherical $L1_2$ precipitates (~ 25 nm, 32.7 vol.%) and blocky $L2_1$ precipitates (~ 200 nm, 3 vol.%) are formed, $L2_1$ precipitates are preferentially formed at subgrain boundaries, and corundum particles grow up to ~ 50 nm	[128]

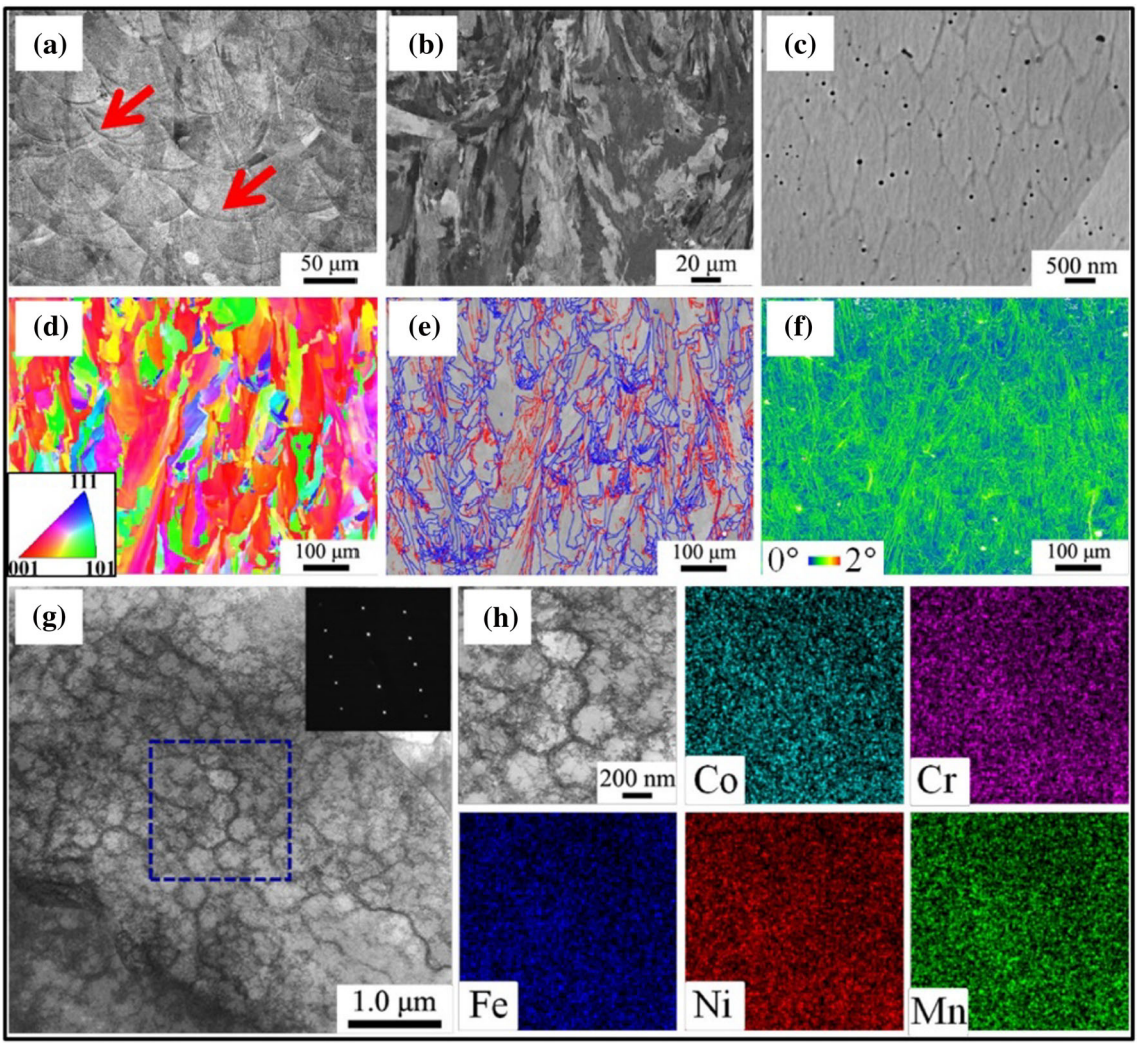

Fig. 6. Hierarchical microstructures of the SLM-ed single-phase CoCrFeMnNi HEA. (a) Melt pools; (b) Columnar grains growing along the build direction; (c) Cellular substructures within grains; (d) EBSD IPF, (e) EBSD image quality map superimposed with high angle grain boundaries (HAGBs)in blue and low angle grain boundaries (LAGBs) in red, (f) EBSD Kernel average misorientation (KAM) maps; (g) Dislocation networks, and (h) elemental distribution maps. (a)–(h). Reproduced with permission from Ref 81 (Color figure online)

strength and ductility, as well as different failure modes (see Fig. 8c and d).

The cellular structures are ubiquitous in AM-ed CoCrFeMnNi HEAs. Their sizes, however, vary significantly due to different cooling rates. The SLM process is characterized by a cooling rate up to 10^6 K/s, leading to the formation of ultra-fine cellular structures of several hundred nanometers.[81, 83, 108] In contrast, the cooling rate of the DED process is less pronounced (10^3-10^4 K/s), and thus, the DED-ed CoCrFeMnNi HEAs often exhibit coarser cellular structures with sizes of 2-5 μm.[39, 88, 109] The cooling rate also influences the elemental segregation kinetics. For example, in the study of Haase et al.[111] and Guan et al.,[39] the segregation of Mn and Ni in the last solidified regions (i.e., cellular boundaries) and the segregation of Co, Cr, and Fe in the initially solidified regions (i.e., cell interiors) have been predicted and validated in numerous DED-ed CoCrFeMnNi HEAs.[39, 88] In contrast, the segregation kinetics are suppressed, and a homogeneous elemental distribution is achieved in SLM-ed CoCrFeMnNi HEAs.[81, 108] The dislocation configurations may also be influenced by cooling rates. Instead of the highly tangled dislocation networks in the SLM-ed CoCrFeMnNi HEA (Fig. 8g), the dislocations in the DED-ed CoCrFeMnNi HEAs are much more loosely arranged.[22, 39, 112] The absence of highly tangled dislocation networks is mainly because the DED process often generates smaller internal stresses and hence, lower dislocation densities, as compared to the SLM process.

As shown above, distinct microstructural features of the AM-ed CoCrFeMnNi HEAs may be achieved via the manipulation of the AM-processing protocol, which in turn

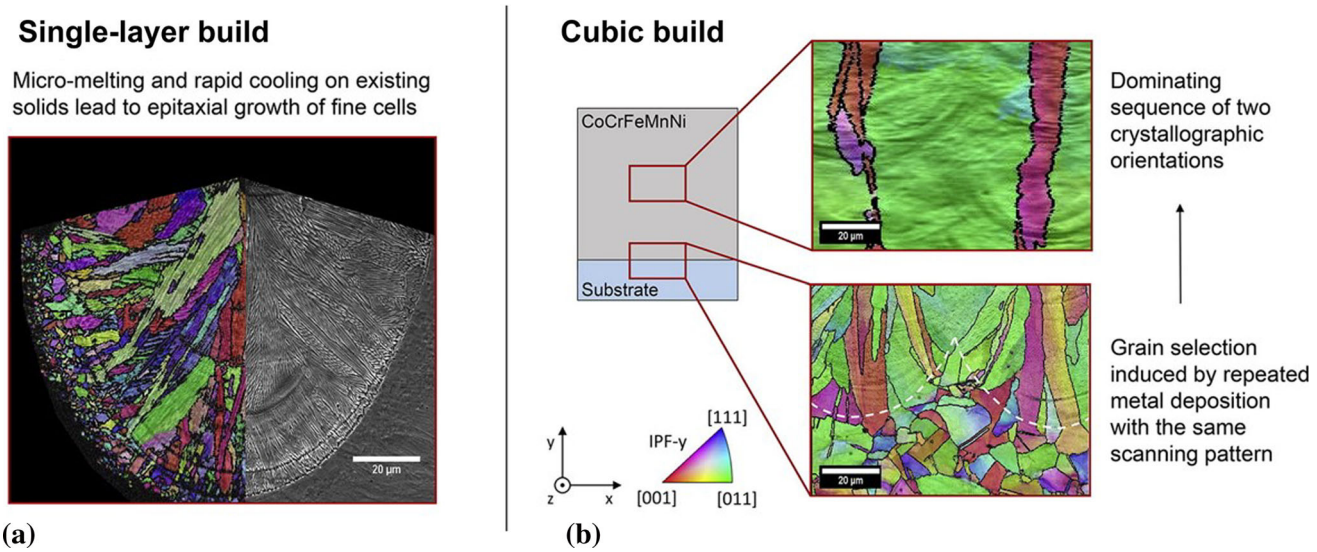

Fig. 7. Microstructures of SLM-ed (a) single-track and (b) multi-track multi-layer CoCrFeMnNi builds. (a)–(b). Reproduced with permission from Ref 83

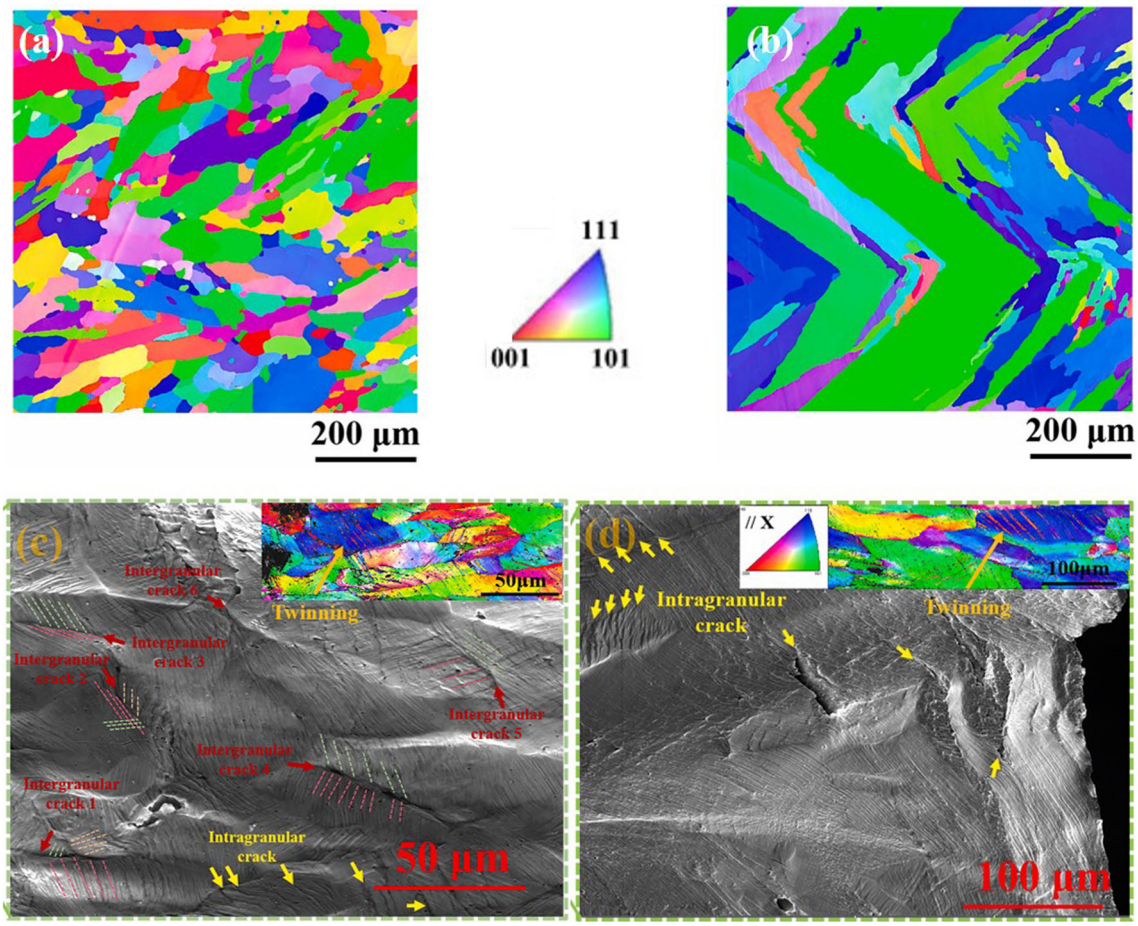

Fig. 8. Microstructures of DED-ed CoCrFeMnNi builds processed at (a), (c) 3 mm/s and (b), (d) 4 mm/s. (a), (b) Microstructures prior to tension, and (c), (d) microstructures after tension fracture. (a)–(d). Reproduced from permission from Ref 110

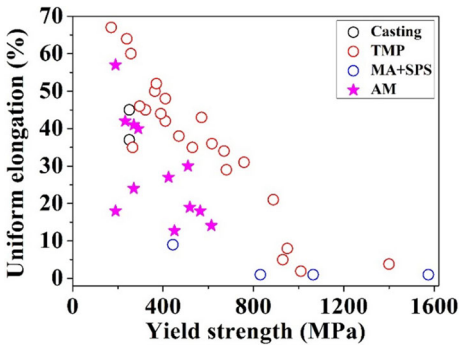

Fig. 9. A summary of uniform tensile elongation versus tensile yield strength of CoCrFeMnNi HEAs processed via diverse routes, including casting,[85, 113] TMP,[4, 114–116] mechanical alloying plus spark plasma sintering (MA + SPS),[140] and AM[53, 81, 85, 88, 89, 141] processes

leads to a wide range of tensile properties, e.g., tensile yield strength of ~ 200-600 MPa and uniform tensile elongation of ~ 20-60%.[39, 84–88] Figure 9 compares the tensile properties of CoCrFeMnNi HEAs produced by diverse routes, including casting, TMP, conventional powder metallurgy, and AM processes. The as-cast CoCrFeMnNi HEAs have low tensile yield strengths due to their coarse grains (grain size: hundreds of μm).[85, 113] In contrast, the tensile yield strengths of TMP-ed CoCrFeMnNi HEAs vary from ~ 200 to ~ 1400 MPa.[4, 114–116] Such a wide property space originates form the easy control of the grain size and dislocation density via TMP. Nevertheless, the general strength-ductility trade-off is observed among these samples. For instance, the nanocrystalline TMP-ed CoCrFeMnNi HEAs can realize ultra-high yield strengths over 1 GPa, but the uniform tensile ductility often falls to a few percent or even reaches near zero.

Besides those energy-intensive AM approaches, the DIW process has also been used to print the CoCrFeMnNi HEA. For example, Peng et al. additively manufactured a series of CoCrFeMnNi micro-lattices based on DIW of a specially-designed ink.[32] The ink includes organic solvents, CoCrFeMnNi pre-alloyed particles (15-32 μm), and an organic polymer binder. Such a colloidal suspension ink shows a typical shear-thinning characteristic and has a viscosity of 10^2-10^5 Pa·s, ensuring the formation of continuous filaments and the subsequent drying and shape retention. After a multi-step heat treatment, the thermally sintered CoCrFeMnNi lattices exhibit fully-equiaxed microstructures. The formation of the fully-equiaxed microstructure after sintering allows for the mitigation of the thermal stress, as occurred in other rapid solidification-based AM approaches. Furthermore, these micro-lattices exhibit an exceptional energy absorption due to the substantial and sustained the strain-hardening capability. Similarly, the DIW process has been used to print CoCrFeNi HEA micro-lattices.[117] The formulated ink consists of a blend of nanoscale oxide powders (i.e., Co_3O_4, Cr_2O_3, Fe_2O_3, and NiO) plus several organic substances as the solvent, binder, plasticizer, and surfactant (see Fig. 10a, b, and c). The co-reduction, inter-diffusion, and sintering of these nano-scale oxide particles take place in a subsequent heat treatment under the H_2/Ar atmosphere, leading to the formation of fully annealed and dense CoCrFeNi lattices (Fig. 10d). Such CoCrFeNi lattices also exhibit excellent compressive properties at both ambient and cryogenic temperatures (Fig. 10e).

3.1.2 FCC HEAs Reinforced with Ceramic Particles

Single-phase FCC HEAs (e.g., CrMnFeCoNi and CrFeCoNi) often exhibit low yield strengths (Fig. 11). Hence, numerous efforts have been devoted to strengthening these single-phase FCC HEAs. One effective approach is to introduce secondary hard ceramic particles. For example, in a study by Park et al.,[53] a C-doped CoCrFeMnNi HEA was printed via SLM from CoCrFeMnNi prealloyed particles with additions of 1 atom-percent (at.%) carbon. Interestingly, the precipitation of nanoscale Mn-rich oxides and sulfides and Cr-rich carbides was activated in this SLM-ed C-doped CoCrFeMnNi HEA, and these nano-precipitates tend to form along the cellular boundaries. It was found that at a higher laser scan speed, V, a smaller number of carbides were achieved, i.e., ~ 1.73 volume percent (vol.%) for V = 200 mm/s versus ~ 1.13 vol.% for V = 600 mm/s. This trend may be due to a shorter exposure time for carbide formation when the laser scan speed is too high. In a study by Kim et al.,[118] the CoCrFeMnNi HEA was also fabricated via SLM and its high-cycle fatigue properties were investigated. In addition to the common features like refined grains and cellular structures, some in-situ Mn_2O_3 oxides were also observed at cellular boundaries (Fig. 12a, b, and c). The formation of these oxides is ascribed to the existence of trace oxygen (419 ppm) in the starting powder particles. The SLM-ed CoCrFeMnNi HEA reinforced with these in-situ formed Mn_2O_3 oxides exhibits significantly enhanced fatigue properties, as compared with the conventionally processed counterpart, i.e., fatigue strength of 570 versus 280 MPa (Fig. 12d). Furthermore, the deformation twinning activated during cyclic loading also contributes to the excellent fatigue properties of the SLM-ed CoCrFeMnNi HEA (Fig. 12e). More research on the AM-ed C-doped HEAs can be found in Ref 119.

In addition to the design approach of in-situ nanoceramic precipitates, composites comprised of HEA pre-alloyed particles and foreign ceramic particles such as TiN,[120–122] WC,[118, 123] TiC[118, 124] have also been studied. In Refs 120–122, a mixture of pre-alloyed CoCrFeMnNi particles and TiN nano-particles AM-ed via SLM,

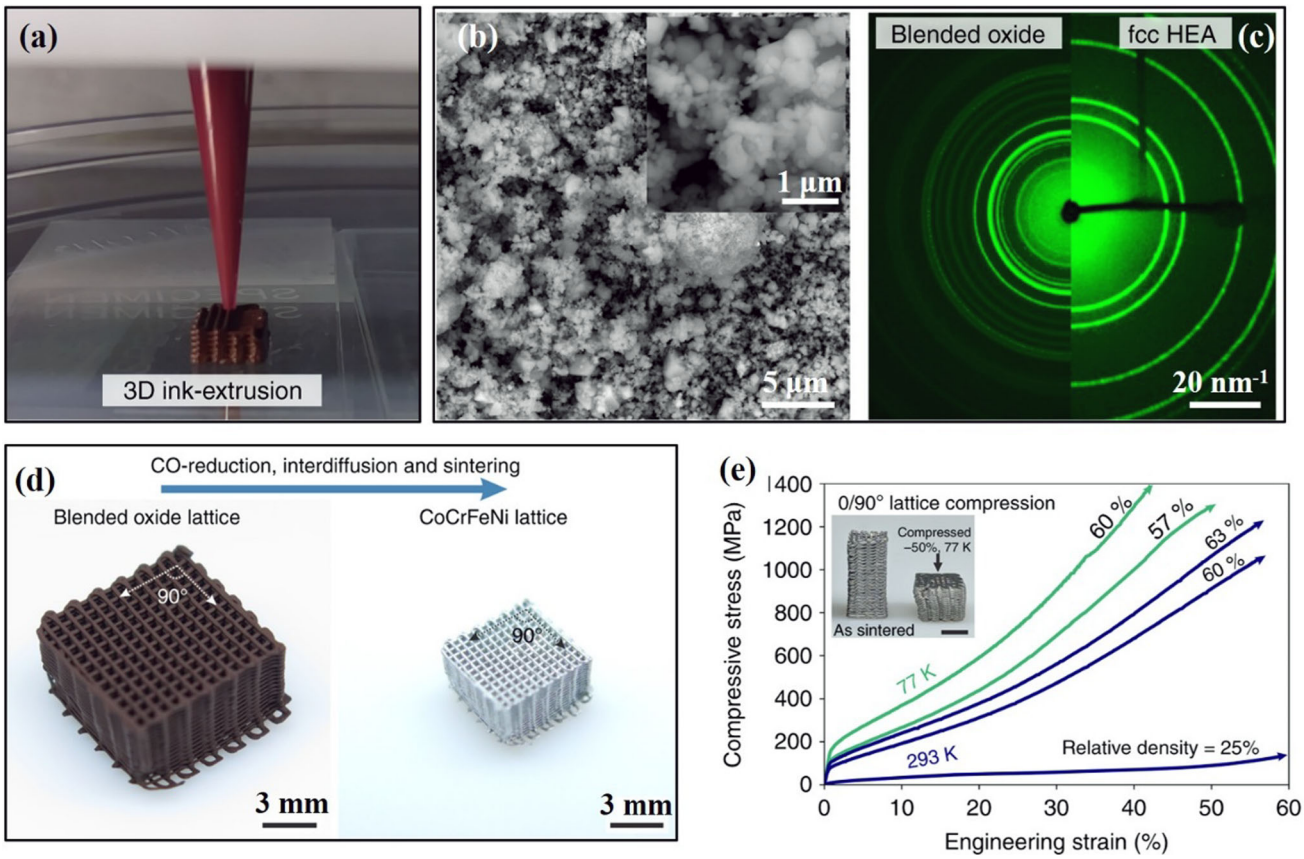

Fig. 10. 3D printing of CoCrFeNi lattices via (a) DIW from (b), (c) a blend of oxide particles. (d) Co-reduction, inter-diffusion, and sintering of oxide particles, leading to a fully annealed, metallic CoCrFeNi lattice with a high relative density. (e) Excellent mechanical properties at ambient and cryogenic temperatures. (a)–(e). Reproduced with permission from Ref 117

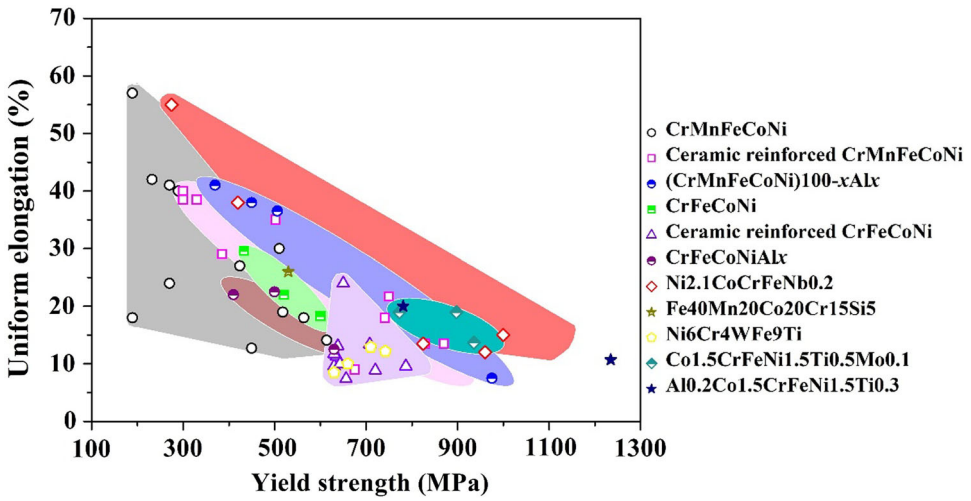

Fig. 11. A summary of the tensile yield strength versus uniform tensile elongation of various 3D-printed HEAs[53, 81, 85, 88, 89, 96–98, 119, 123–127, 132, 138, 141–147]

and it was found that the SLM-ed CoCrFeMnNi/TiN composites show a nearly equiaxed microstructure with grain sizes down to a few micrometers. Such equiaxed microstructures are totally different from the SLM-ed CoCrFeMnNi HEA that often shows columnar microstructures. These TiN nanoparticles are preferentially located at grain boundaries. The present authors believe that these TiN nanoparticles are not melted during printing

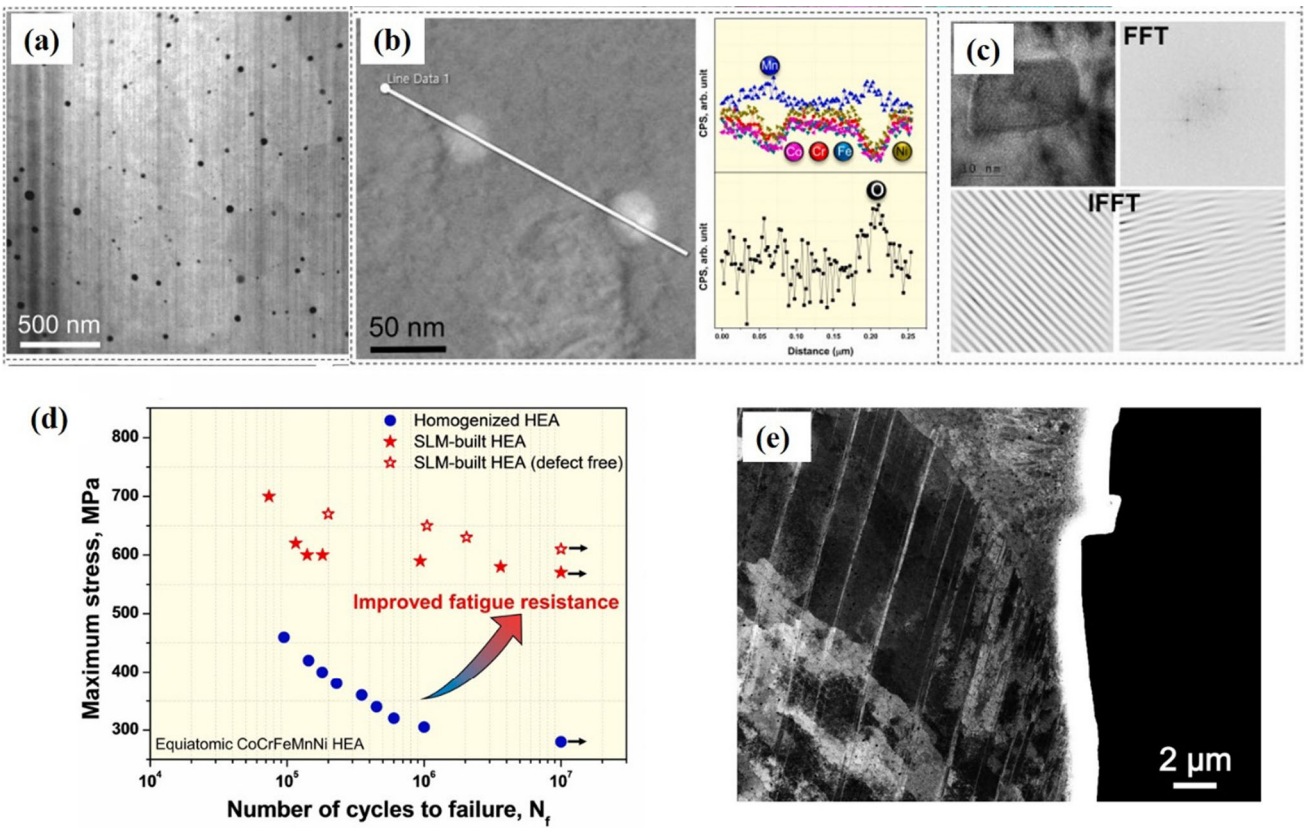

Fig. 12. (a) Nano-precipitates at cellular walls. (b), (c) Determination of nanoprecipitates to be Mn_2O_3. (d) S-N curves of SLM-ed and conventionally processed CoCrFeMnNi HEAs. (e) A high density of deformation twins at the specimen surface after failure. (a)–(e). Reproduced with permission from Ref 118

due to its high melting point and the relative low energy density intrinsic to the SLM process. Consequently, these TiN nanoparticles are eventually rejected to the last solidified regions (i.e., grain boundaries). Similar findings were also reported in Ref 124.

3.1.3 FCC HEAs Reinforced with Intermetallic Precipitates

Another effective approach to strengthen these single-phase FCC HEAs is to promote precipitation hardening. In an investigation by Gao et al.,[125] a series of HEAs $(CoCrFeMnNi)_{100-x}Al_x$ (x = 0, 2, 5, and 8) were fabricated via DED from pre-alloyed CoCrFeMnNi particles and elemental Al particles. In contrast to the single-phase FCC microstructure of the $(CoCrFeMnNi)_{98}Al_2$ HEA, a dual-phase microstructure consisting of the FCC matrix and BCC precipitates was achieved in both $(CoCrFeMnNi)_{95}Al_5$ and $(CoCrFeMnNi)_{92}Al_8$ HEAs. Therefore, precipitation-strengthening mechanisms can be activated. Further increasing the Al content leads to an increase in the strength but a decrease in the ductility. However, the $(CoCrFeMnNi)_{100-x}Al_x$ occupies a strength-ductility domain that is located at the upper right side of the single-phase FCC CoCrFeMnNi HEA, indicating that an enhanced strength-ductility synergy is achieved via precipitation strengthening (Fig. 11). Similarly, another precipitation-hardened HEA $CoCrFeNiAl_{0.3}$ was also printed, and after aging at 620 °C for 50 h, some nano-scale spherical and tubular $L1_2$ precipitates were formed within the grain interior, together with some B2 and σ precipitates preferentially along the grain boundaries.[126] In a study by Zhou et al.,[127] another precipitation-hardened $Ni_{2.1}CoCrFeNb_{0.2}$ HEA was printed, where Nb was introduced into the $Ni_{2.1}CoCrFe$ matrix to promote the formation of γ'' Ni_3Nb ($D0_{22}$ ordered) precipitates upon post-heat treatment. Furthermore, a specific orientation relationship was observed between the γ'' precipitates and the FCC γ matrix, $<001>_{\gamma''}//<011>_{\gamma}$ and $(100)_{\gamma''}//(100)_{\gamma}$.

More recently, Lin et al. additively manufactured via SLM another precipitation-hardened $Al_{0.2}Co_{1.5}CrFeNi_{1.5}Ti_{0.3}$ HEA.[128] The cellular structures (~ 527 nm) and corundum particles (~ 5 nm) were observed in this SLM-ed $Al_{0.2}Co_{1.5}CrFeNi_{1.5}Ti_{0.3}$ HEA (Fig. 13a and b). The post-aging treatment at 750 °C for 50 h promotes the formation of both spherical $L1_2$-ordered precipitates (~ 25

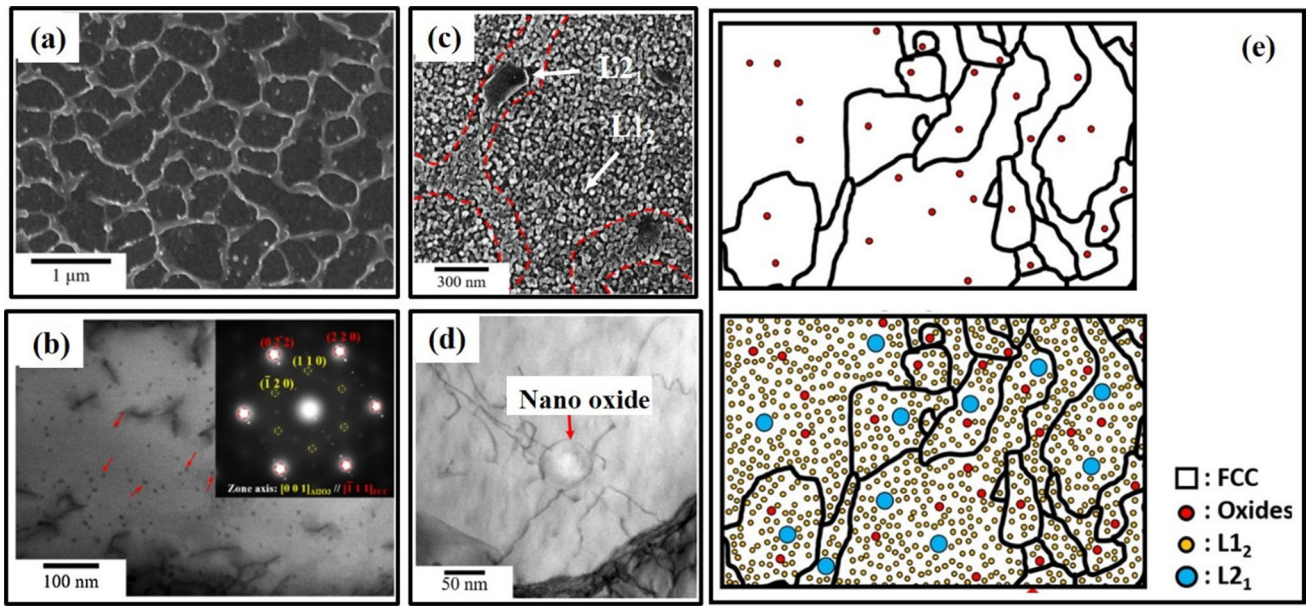

Fig. 13. 3D printing of a precipitation hardened HEA $Al_{0.2}Co_{1.5}CrFeNi_{1.5}Ti_{0.3}$ via SLM. SEM micrographs showing (a) cellular structures and (b) corundum particles of the SLM-ed $Al_{0.2}Co_{1.5}CrFeNi_{1.5}Ti_{0.3}$ HEA. (c) Precipitation of $L1_2$-ordered precipitates and $L2_1$-ordered precipitates during aging. (d) Corundum particles in the aged $Al_{0.2}Co_{1.5}CrFeNi_{1.5}Ti_{0.3}$ HEA. (e) Schematic illustrations presenting the precipitation process during aging. (a)–(e). Reproduced with permission from Ref 128

nm) and blocky $L2_1$-ordered precipitates ($\sim$ 200 nm) (Fig. 13c). These blocky $L2_1$-ordered precipitates preferentially form at sub-grain boundaries (Fig. 13c). Furthermore, the post-aging treatment also promotes the growth of the corundum particles, with the particle size increased to $\sim$ 50 nm (Fig. 13d). The precipitation process is schematically shown in Fig. 13(e), and this process contributes to the tensile properties significantly. More specifically, both the tensile yield strength and ultimate tensile strength increase by $\sim$ 500 MPa, reaching 1235 and 1550 MPa, respectively. Revisiting Fig. 11, these precipitation-hardened HEAs show the best strength-ductility synergy among all the reported 3D-printed HEAs up to date.

3.2 BCC-Based HEAs

Refractory HEAs, often consisting of refractory BCC metals and crystallizing as a single-phase BCC solid-solution structure, have also been frequently printed.[51] In addition to those BCC metals (e.g., W, Mo, Nb, Ta, and V), some allotropic metals (e.g., Hf, Zr, and Ti) are also common elements in refractory HEAs. Refractory HEAs have aroused considerable attention because of their high melting points, high strengths, and excellent thermal stability at elevated temperatures. Thus far, refractory HEAs are mainly fabricated via vacuum arc melting and casting due to the ultra-high melting points of constituent elements of refractory HEAs. However, the difference in the melting point of each constituent element may be very large, e.g., 1668 °C for Ti and 3017 °C for Ta. Such a large melting-point difference possibly leads to the evaporation of low melting point metals during arc-melting and hence, results in the deviation of the achieved composition from the designed one. Severe elemental segregation and coarse dendritic grains of the as-cast refractory HEAs may also deteriorate their thermal stability and mechanical properties. In addition, the high strength and limited plasticity of refractory HEAs make post-machining or -processing difficult. Hence, a strong interest has been recently driven in the fabrication of refractory HEAs via the AM process.

Till today, refractory HEAs are often printed from mixtures of elemental powders, and the majority of the research is focused on the microstructure, hydrogen-storage properties, and corrosion resistance of AM-ed refractory HEAs.[51, 100, 102, 129] The mechanical properties (e.g., tensile, compressive) of the AM-ed refractory HEAs are rarely reported, possibly due to the high cracking sensitivity of refractory HEAs. Very recently, in a study of Zhang et al.,[130] a novel refractory HEA was successfully designed and printed via SLM, without any cracks, and its compressive properties were tested. As can be seen from Fig. 14(a), the SLM-ed NbMoTa HEA exhibits severe cracking, but fortunately the addition of Ti and Ni shows some beneficial effects. The addition of Ti reduces the crack size, and the addition of Ni can eliminate the

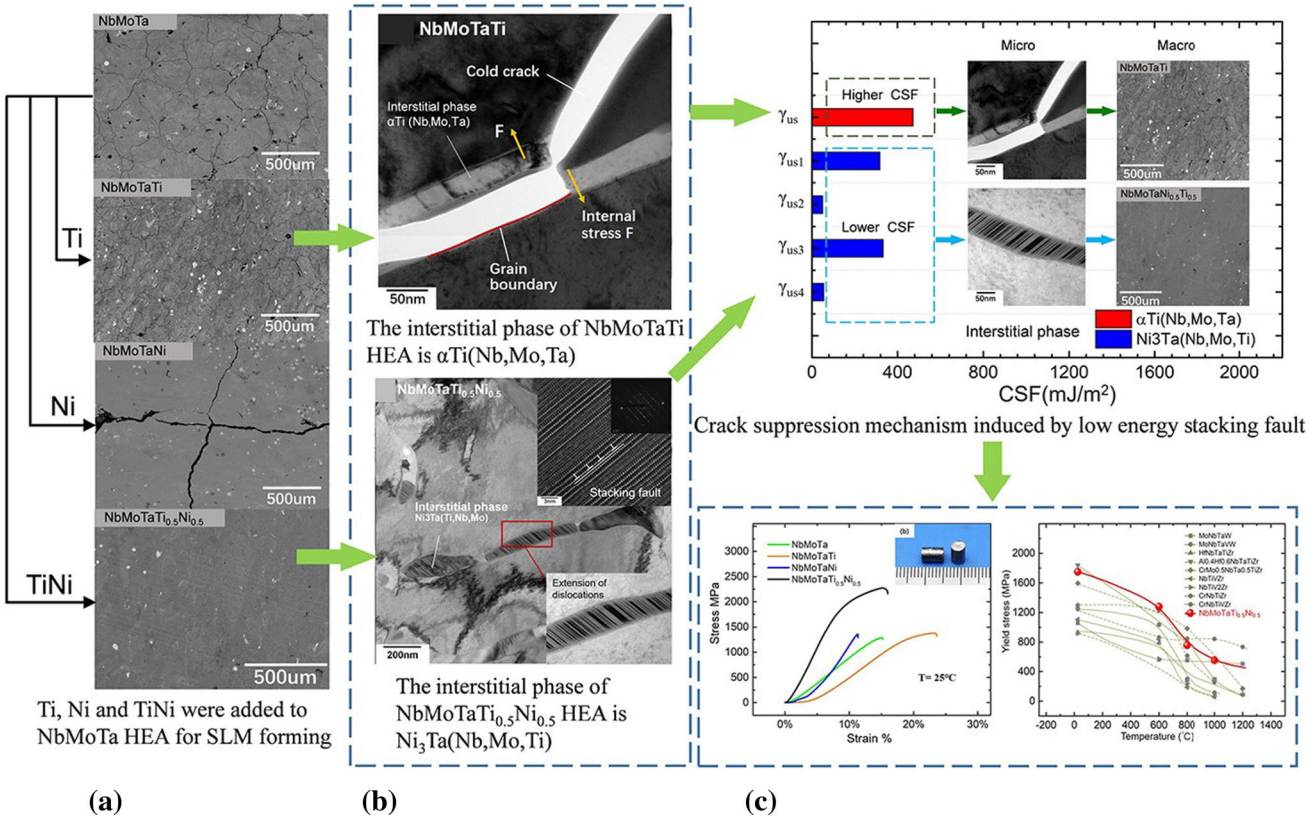

Fig. 14. (a) SEM micrographs of NbMoTa, NbMoTaTi, NbMoTaNi, and $NbMoTaTi_{0.5}Ni_{0.5}$ HEAs, showing the formation of the cracks. (b) TEM images showing the grain-boundary phases and crystallographic defects (e.g., dislocations). (c) Crack-suppression mechanisms and compressive properties. (a)–(c). Reproduced with permission from Ref 130

majority of microcracks. Interestingly, the simultaneous addition of Ti and Ni completely suppresses the formation of cracks in the SLM-ed $NbMoTaTi_{0.5}Ni_{0.5}$ (Fig. 14a). The suppressed cracking phenomenon observed in the SLM-ed $NbMoTaTi_{0.5}Ni_{0.5}$ may be ascribed to the beneficial grain-boundary phases (Fig. 14b and c). The grain boundaries of the SLM-ed $NbMoTaTi_{0.5}Ni_{0.5}$ HEA are decorated with the Ni_3Ta (Ti, Nb, Mo) phase, which has a lower stacking fault energy (SFE). As such, when exposed with the internal stresses during cooling, dislocation reaction occurs more readily, e.g., the formation of extended dislocations. Also, stacking fault regions can consume energy during grain-boundary slip, thus avoiding the separation of grain-boundary phases. In this way, the cracking behavior is suppressed in the SLM-ed $NbMoTaTi_{0.5}Ni_{0.5}$ HEA. Furthermore, the excellent compressive properties are achieved in this SLM-ed $NbMoTaTi_{0.5}Ni_{0.5}$ HEA (Fig. 14c). It is worth noting, however, that the tensile properties of AM-ed refractory HEAs have not been reported to date, and 3D printing of high-performance refractory HEAs with a superior combination of tensile strength and ductility represents a significant future direction.

3.3 HEAs with TRIP Effects

In certain HEAs, additional deformation mechanisms (e.g., TRIP) can be activated during straining, which is beneficial for sustained work hardening and hence, a simultaneous enhancement of strength and ductility.[131] The TRIP effect often originates from the low SFE value of the matrix phase and thus, the high driving force for phase transformation. TRIP HEAs have attracted increasing attention for printing in recent years. In a study by Agrawal et al.,[132] SLM was used to produce a TRIP HEA $Fe_{40}Mn_{20}Co_{20}Cr_{15}Si_5$. Figure 15 shows the microstructure and tensile properties of this SLM-ed HEA $Fe_{40}Mn_{20}Co_{20}Cr_{15}Si_5$. For comparative purposes, the microstructure and tensile properties of the as-cast counterpart were also presented. Surprisingly, the as-printed $Fe_{40}Mn_{20}Co_{20}Cr_{15}Si_5$ shows an increased strength and ductility simultaneously. The enhanced strength partly originates from the refined grain size (i.e., ~ 30 μm of the as-printed material versus ~ 100 μm of the as-cast counterpart), and another important contributor is the high density of dislocations in the as-printed material. It is also interesting to note that the as-printed material shows a dual-phase microstructure, i.e., ~

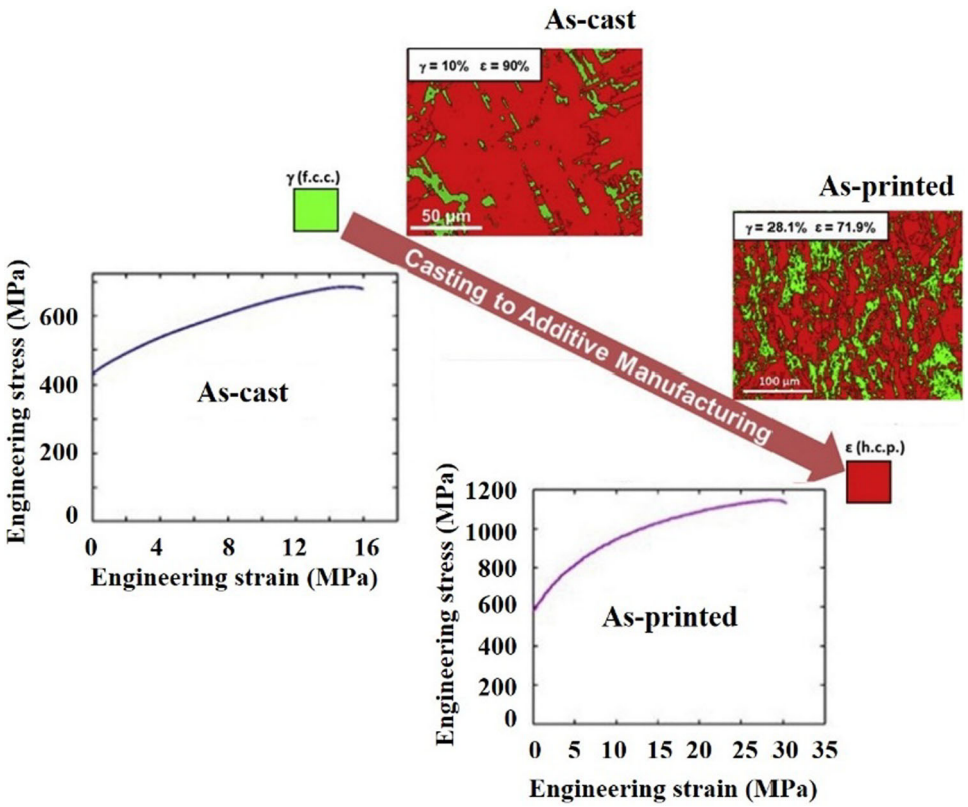

Fig. 15. The comparison of microstructures and tensile properties between the as-cast and as-printed $Fe_{40}Mn_{20}Co_{20}Cr_{15}Si_5$. Reproduced from permission from Ref 132

72% ε (HCP) phase and $\sim$ 28% γ (FCC) phase. In contrast, the as-cast counterpart has a $\sim$ 90% ε (HCP) phase and $\sim$ 10% γ (FCC) phase. The more metastable microstructure of the as-printed $Fe_{40}Mn_{20}Co_{20}Cr_{15}Si_5$ HEA can be ascribed to the high cooling rate associated with the SLM process. During tensile straining of this SLM-ed $Fe_{40}Mn_{20}Co_{20}Cr_{15}Si_5$ HEA, the uniform strain accommodation in both phases occurs. The γ phase accommodates strain via TRIP, leading to the γ phase-fraction decrease from initial $\sim$ 28 to $\sim$ 9% at failure. The more pronounced TRIP effect of the SLM-ed $Fe_{40}Mn_{20}Co_{20}Cr_{15}Si_5$ HEA contributes to the more sustained working hardening and hence, improved ductility. As mentioned previously, the activation of the TRIP effect is determined by the SFE value. Thus, the stability of a specific HEA can be tuned via compositional modification and SFE engineering. In an investigation by Thapliyal et al.,[133] SLM was used to produce the $Fe_{38.5}Mn_{20}Co_{20}Cr_{15}Si_5Cu_{1.5}$ HEA. As compared with the aforementioned $Fe_{40}Mn_{20}Co_{20}Cr_{15}Si_5$ HEA, small amounts of Fe were replaced with Cu, leading to a more stable γ matrix. Consequently, the SLM-ed $Fe_{38.5}Mn_{20}Co_{20}Cr_{15}Si_5Cu_{1.5}$ achieves a near single-phase microstructure ($\sim$ 99% γ phase and $\sim$ 1% ε phase). Consistent with the findings of Agrawal et al.,[132] the SLM-ed $Fe_{38.5}Mn_{20}Co_{20}Cr_{15}Si_5Cu_{1.5}$ HEA is more metastable, as compared with the as-cast counterpart ($\sim$ 87% γ phase and $\sim$ 13% ε phase). Also, during tensile straining, a $\sim$ 35% γ phase is transformed into a ε phase.

3.4 Compositionally Graded HEAs

Compositionally graded HEAs with inhomogeneities in compositions, microstructures, and properties have aroused increasing attention. Compositionally- graded HEAs can be used to rapidly explore the desired alloy composition, i.e., high-throughput screening. DED demonstrates a unique advantage in this aspect due to its high flexibility of alloy design by tailoring the feeds of multiple powder feedstocks through multiple co-axial nozzles. For example, in a study by Gwalani et al.,[134] a compositionally-graded HEA $CoCrFeNiAl_x$ (x = 0.3-0.7) along the build direction was additively manufactured via DED, and the microstructures at various locations were investigated. When x = 0.3 ($CoCrFeNiAl_{0.3}$), a single-phase FCC microstructure was observed, which is consistent with the findings of Nartu et al.[126] When x = 0.7 ($CoCrFeNiAl_{0.7}$), an FCC/B2 dual-phase microstructure was achieved. Another example shows that the effect of Al can be found in a study by Borkar et al.[104] In their study, a compositionally graded HEA $Al_xCrCuFeNi_2$ (x = 0-1.5) was additively manufactured via DED. It is found that $Al_xCrCuFeNi_2$ (x = 0) exhibits a single-phase FCC microstructure, whereas the addition of Al promotes a pronounced phase change. For

instance, $Al_{0.4}CrCuFeNi_2$ (x = 0.4) shows an FCC matrix with copious ordered nanoscale $L1_2$ precipitates, i.e., a dual-phase microstructure. In contrast, in $Al_{0.8}CrCuFeNi_2$ (x = 0.8), ordered B2 phases are formed. In another study by Pegues et al.,[135] several types of compositionally-graded HEAs were also additively manufactured via DED. For example, the compositionally graded HEA Nb_x-CoCrFeMnNi was printed, and its composition, microstructure, and properties along the build direction were investigated. A compositional heterogeneity has been established along the build direction, leading to a significant hardness change (Fig. 16a and b). In Fig. 16(b), a summary of the microstructural change along the build direction was also given, e.g., from a near-single-phase FCC microstructure to Nb-rich dendrites or even to cracking. Such microstructural characteristics can be seen from SEM images in Fig. 16(c). Some compositionally graded refractory HEAs have also been studied by AM. In a study by Dobbelstein et al.,[106] a compositionally-graded $Ti_{25}Zr_{50-x}Nb_xTa_{25}$ (x = 0-50) HEA with no cracks was additively manufactured via DED. Unlike the common morphological and crystallographic textures (e.g., columnar microstructures with <100> or <110> textures), fine equiaxed microstructures with grain sizes of several micrometers were observed in a substantial portion of this graded HEA part. It should be pointed out that in another study by Borkar et al.,[104] $Al_xCrCuFeNi_2$ (x = 0-1.5) was also reported to achieve a portion of equiaxed microstructures at specific locations and hence certain compositions. Both studies indicate that in addition to the afore-mentioned $AlCoCrFeNiTi_{0.5}$, numerous alloy compositions can produce equiaxed microstructures, with random crystallographic textures. This feature helps achieve high-performance HEA parts with anisotropic mechanical properties. More research on compositionally-graded HEAs via DED can found in Ref 103.

3.5 Laminated HEAs

Lamination is also an effective approach to achieve the enhanced strength-ductility synergy in HEAs due to several beneficial mechanisms, e.g., crack blunting[136] and crack bridging.[137] In a study by Guan et al.,[40] they additively manufactured via DED a laminated HEA CoCrFeMnNi/$AlCoCrFeNiTi_{0.5}$ that exhibits an enhanced synergy between the compressive strength and macroscopic

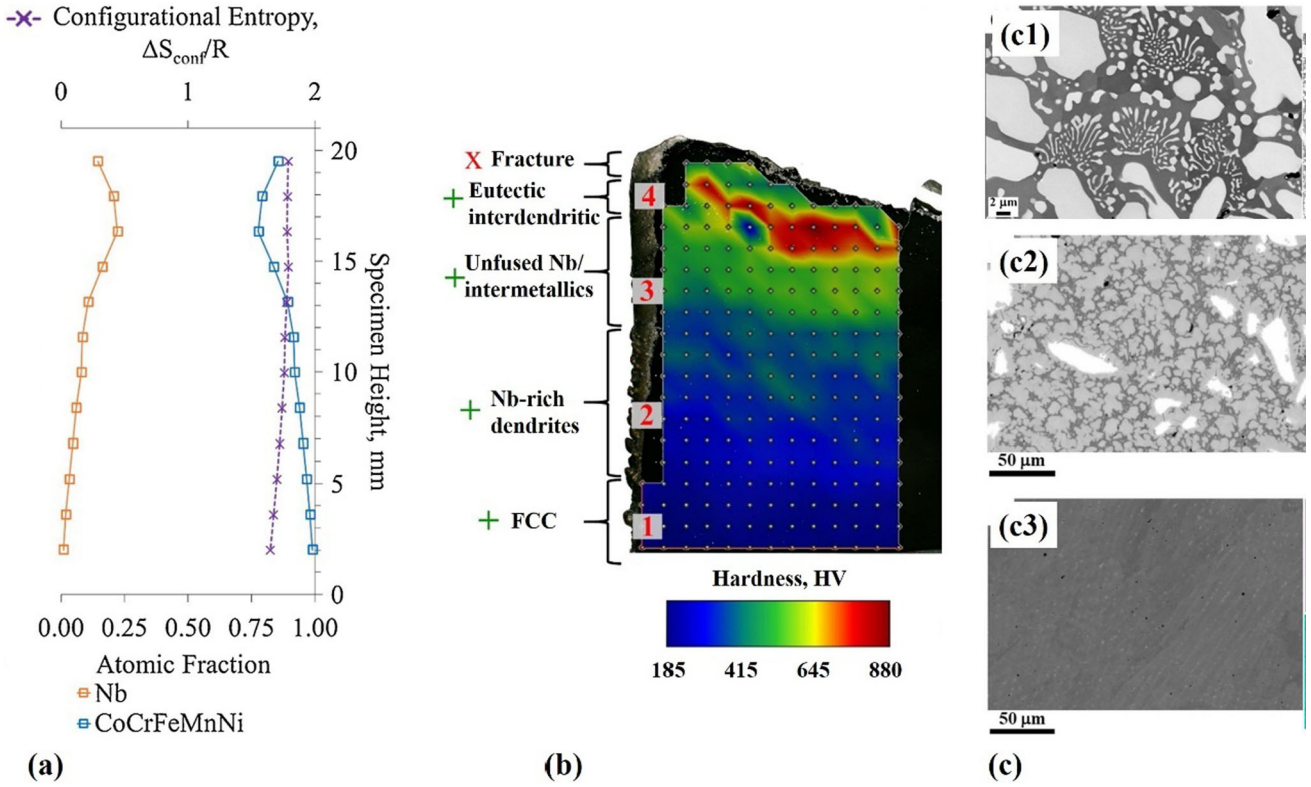

Fig. 16. (a) Compositional and configurational entropy profiles and (b) Hardness overlap map of a compositionally graded NbxCoCrFeMnNi HEA. The microstructural characteristics are summarized in the hardness-overlap map. (c) Representative SEM images showing cracking, unfused Nb particles, and near-single-phase FCC microstructures. (a)–(c). Reproduced with permission from Ref 135

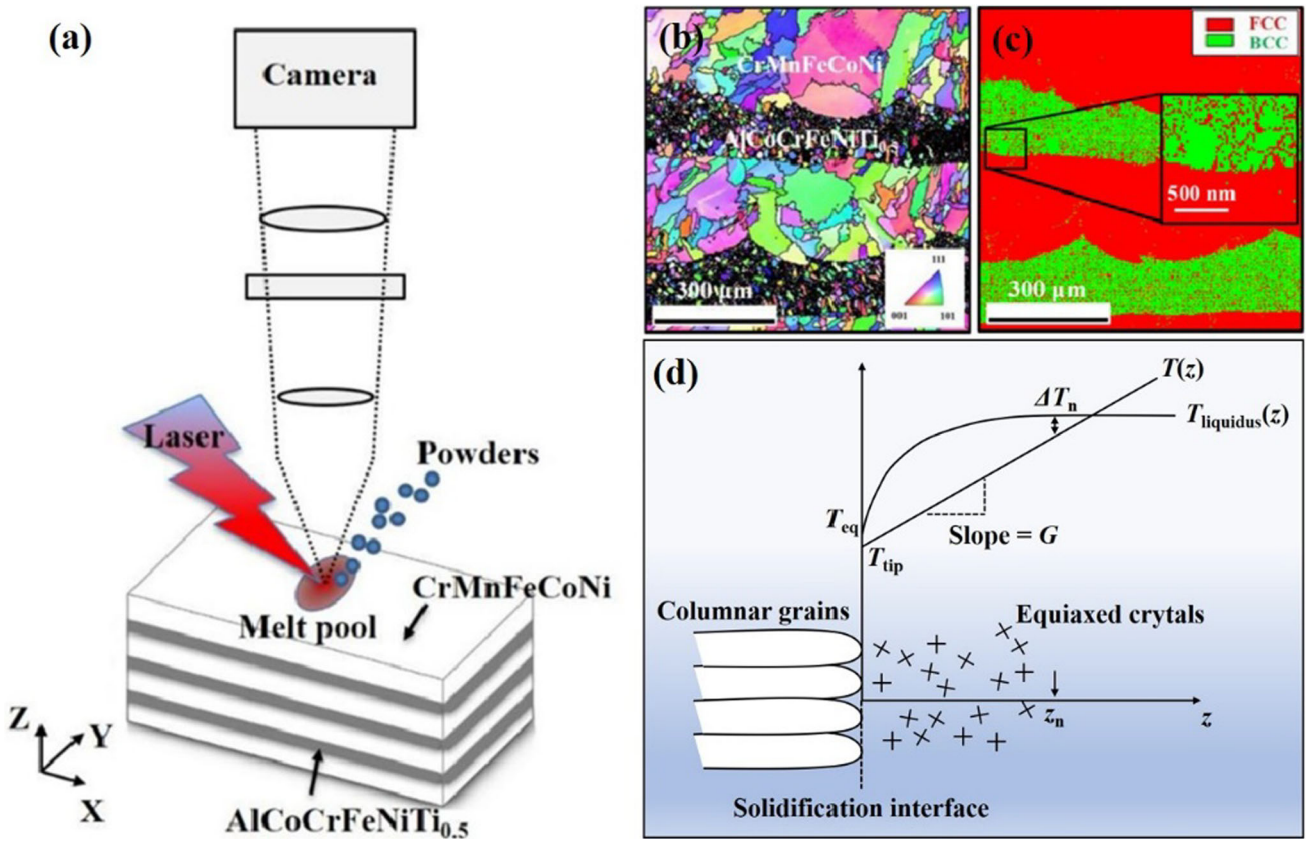

Fig. 17. (a) Schematic of synthesis of a laminated CoCrFeMnNi/$AlCoCrFeNiTi_{0.5}$ HEA via DED. EBSD (b) IPF map, and (c) phase map of the as-deposited laminated HEA showing alternate columnar and equiaxed-grain structures and alternate FCC and BCC phases, respectively. The reference axis for the IPF map is the *z*-axis (i.e., the build direction). (d) Schematic view of the CET phenomenon observed for the as-deposited laminated HEA. (a)–(d). Reproduced with permission from Ref 40

plasticity, surpassing those of monolithic bulk HEAs. As shown in Fig. 17(a), both constituent metallic particles were loaded into two separate powder feeding hoppers and were blown alternately. Hence, a laminated microstructure was achieved (Fig. 17b and c). The high compressive strength of this laminated HEA originates from the hard BCC-structured and equiaxed microstructures in the $AlCoCrFeNiTi_{0.5}$ layers, whereas the large macroscopic plasticity originates from the soft FCC-structured and columnar microstructures in the CoCrFeMnNi layers. It should be noted that the partial remelting during repeated depositions of AM processes can induce some elemental mixing between the two constituent alloys, resulting in the inter-penetrating structure in the vicinity of lamellar interfaces. Furthermore, as mentioned previously, the columnar to equiaxed transition (CET) model can be used to explain the formation of equiaxed microstructures in the $AlCoCrFeNiTi_{0.5}$ lamellae (Fig. 17d). In another study by Cai et al.,[107] a crack-free laminated CoCrFeNi/CoCrFeNiAl HEA was also printed via DED, and an alternating FCC/BCC microstructure was achieved. The laminated CoCrFeNi/CoCrFeNiAl HEA exhibits the enhanced strength-ductility synergy as well, surpassing that of the monolithic CoCrFeNi HEA. Both research outcomes prove that it is feasible to design HEAs with heterogeneous phases/microstructures and enhanced mechanical properties via DED.

4 Conclusions and Perspectives

This paper introduces several metal AM techniques, including DED, SLM, EBM, and DIW. DED, SLM, and EBM are energy-intensive AM approaches that are characterized by rapid solidification and in-situ heating-cooling thermal cycles. Melt-pool solidification often promotes the formation of columnar grain geometries, but some specific external stimuli (e.g., ultrasonic) may facilitate the formation of equiaxed-grained microstructures. In contrast, DIW is an ink extrusion-based AM approach that utilizes post-sintering to achieve fully dense components. Hence, the DIW-ed parts often show equiaxed-grained microstructures with a random crystallographic texture. Thereafter, this paper performs a comprehensive and

critical review on the microstructures and mechanical behavior of AM-ed HEAs. The microstructures of AM-ed single-phase FCC HEAs are highly heterogeneous, consisting of melt pools, columnar grains, cellular structures, dislocations, and elemental segregations on hierarchical length scales. The single-phase FCC HEAs are ductile, but their strengths are insufficient. Hence, numerous efforts have been made to promote the formation of nano-scale precipitates (ceramics and intermetallics) towards an enhanced strength-ductility synergy. Refractory HEAs have also been printed mainly from mixtures of elemental particles, but their tensile and compressive properties are poorly understood. The AM-ed TRIP HEAs experience phase transformations during tensile straining and show enhanced tensile properties, as compared with the as-cast counterparts. Furthermore, DED enables a flexible control on the local composition within a single part and hence, can be used to produce compositionally graded or laminated HEAs. Especially, the DED-ed laminated HEAs exhibit an enhanced strength-ductility compromise, as compared with the monolithic HEAs. These results suggest that DED is a feasible approach to generate laminated HEAs with enhanced properties.

Inspired by these pioneering works, future research activities are suggested here. One possible research direction is to screen and print the multi-phase HEAs with both hard and ductile phases because the existing results show that multi-phase HEAs often achieve an enhanced strength-ductility synergy. The desirable multi-phase HEAs can be selected from existing literature or predicted from thermodynamic simulations. Furthermore, exploring compositions that can induce equiaxed microstructures with random crystallographic textures is also an important research direction. This is critical for the development of high-performance HEA parts with isotropic mechanical properties. Furthermore, the ultrasonic assistance during casting, welding, and 3D printing has been proved to be effective for the control of the microstructure. However, the ultrasonic-assisted 3D printing of HEAs has not been reported to the best of our knowledge and needs to be explored in the future. Last but not the least, the creep properties, fracture toughness, fatigue properties, irradiation resistance, and oxidation resistance of the AM-ed HEAs need to be explored to proliferate the structural utility of the AM-ed HEAs.

Acknowledgment W.C. acknowledges the financial support from the US National Science Foundation (CMMI-1927621 and DMR-2004429) and UMass Faculty Startup. P.K.L. very much appreciates the supports from (1) the U.S. Army Office Project (W911NF-13-1-0438 and W911NF-19-2-0049) with the program managers, Drs. Michael P. Bakas, David M. Stepp, and S. Mathaudhu, and (2) the National Science Foundation (DMR-1611180 and 1809640) with the program directors, Drs. Judith Yang, Gary Shiflet, and Diana Farkas.

References

1. B. Cantor, I.T.H. Chang, P. Knight, and A.J.B. Vincent, Microstructural Development in Equiatomic Multicomponent Alloys, *Mater. Sci. Eng. A*, 2004, **375–377**, p 213–218.
2. J.W. Yeh, S.K. Chen, S.J. Lin, J.Y. Gan, T.S. Chin, T.T. Shun, C.H. Tsau, and S.Y. Chang, Nanostructured High-Entropy Alloys with Multiple Principal Elements: Novel Alloy Design Concepts and Outcomes, *Adv. Eng. Mater.*, 2004, **6**, p 299–303.
3. Y.-J. Liang, L. Wang, Y. Wen, B. Cheng, Q. Wu, T. Cao, Q. Xiao, Y. Xue, G. Sha, Y. Wang, Y. Ren, X. Li, L. Wang, F. Wang, and H. Cai, High-Content Ductile Coherent Nanoprecipitates Achieve Ultrastrong High-Entropy Alloys, *Nat. Commun.*, 2018, **9**, p 4063.
4. B. Gludovatz, A. Hohenwarter, D. Catoor, E.H. Chang, E.P. George, and R.O. Ritchie, A Fracture-Resistant High-Entropy Alloy for Cryogenic Applications, *Science*, 2014, **345**, p 1153–1158.
5. Z. Wu, H. Bei, G.M. Pharr, and E.P. George, Temperature Dependence of the Mechanical Properties of Equiatomic Solid Solution Alloys with Face-Centered Cubic Crystal Structures, *Acta Mater.*, 2014, **81**, p 428–441.
6. N.A.P.K. Kumar, C. Li, K.J. Leonard, H. Bei, and S.J. Zinkle, Microstructural Stability and Mechanical Behavior of FeNiMnCr High Entropy Alloy Under Ion Irradiation, *Acta Mater.*, 2016, **113**, p 230–244.
7. S. Maiti, and W. Steurer, Structural-Disorder and Its Effect on Mechanical Properties in Single-Phase TaNbHfZr High-Entropy Alloy, *Acta Mater.*, 2016, **106**, p 87–97.
8. O.N. Senkov, G.B. Wilks, J.M. Scott, and D.B. Miracle, Mechanical Properties of $Nb_{25}Mo_{25}Ta_{25}W_{25}$ and $V_{20}Nb_{20}Mo_{20}Ta_{20}W_{20}$ Refractory High Entropy Alloys, *Intermetallics*, 2011, **19**, p 698–706.
9. M.C. Gao, B. Zhang, S.M. Guo, J.W. Qiao, and J.A. Hawk, High-Entropy Alloys in Hexagonal Close-Packed Structure, *Metall. Mater. Trans. A*, 2016, **47**, p 3322–3332.
10. A. Takeuchi, K. Amiya, T. Wada, K. Yubuta, and W. Zhang, High-Entropy Alloys with a Hexagonal Close-Packed Structure Designed by Equi-atomic Alloy Strategy and Binary Phase Diagrams, *JOM*, 2014, **66**, p 1984–1992.
11. X.Z. Gao, Y.P. Lu, B. Zhang, N.N. Liang, G.Z. Wu, G. Sha, J.Z. Liu, and Y.H. Zhao, Microstructural Origins of High Strength and High Ductility in an $AlCoCrFeNi_{2.1}$ Eutectic High-Entropy Alloy, *Acta Mater.*, 2017, **141**, p 59–66.
12. P.J. Shi, W.L. Ren, T.X. Zheng, Z.M. Ren, X.L. Hou, J.C. Peng, P.F. Hu, Y.F. Gao, Y.B. Zhong, and P.K. Liaw, Enhanced Strength-Ductility Synergy in Ultrafine-Grained Eutectic High-Entropy Alloys by Inheriting Microstructural Lamellae, *Nat. Commun.*, 2019, **10**, p 1–8.
13. W. Zhang, L. Liu, S. Peng, J. Ren, F. Wu, J. Shang, M. Chen, Y. Zhang, Z. Zhao, J. Qi, B. Wang, and W. Chen, The Tensile Property and Notch Sensitivity of AlCoCrFeNi2.1 High Entropy Alloy with a Novel "Steel-Frame" Eutectic Microstructure, *J. Alloys Compd.*, 2021, **863**, p 158747.
14. K. Yao, L. Liu, J. Ren, Y. Guo, Y. Liu, Y. Cao, R. Feng, F. Wu, J. Qi, J. Luo, P.K. Liaw, and W. Chen, High-Entropy Intermetallic Compound with Ultra-High Strength and Thermal Stability, *Scr. Mater.*, 2021, **194**, p 113674.
15. P. Lu, J.E. Saal, G.B. Olson, T. Li, O.J. Swanson, G.S. Frankel, A.Y. Gerard, K.F. Quiambao, and J.R. Scully, Computational Materials Design of a Corrosion Resistant High Entropy Alloy for Harsh Environments, *Scr. Mater.*, 2018, **153**, p 19–22.
16. Y. Shi, L. Collins, R. Feng, C. Zhang, N. Balke, P.K. Liaw, and B. Yang, Homogenization of AlxCoCrFeNi High-Entropy

Alloys with Improved Corrosion Resistance, *Corros. Sci.*, 2018, **133**, p 120–131.
17. Z. Tang, T. Yuan, C.-W. Tsai, J.-W. Yeh, C.D. Lundin, and P.K. Liaw, Fatigue Behavior of a Wrought $Al_{0.5}CoCrCuFeNi$ Two-Phase High-Entropy Alloy, *Acta Mater.*, 2015, **99**, p 247–258.
18. Z. Wu, H. Bei, F. Otto, G.M. Pharr, and E.P. George, Recovery, Recrystallization, Grain Growth and Phase Stability of a Family of FCC-Structured Multi-component Equiatomic Solid Solution Alloys, *Intermetallics*, 2014, **46**, p 131–140.
19. W. Ji, W.M. Wang, H. Wang, J.Y. Zhang, Y.C. Wang, F. Zhang, and Z.Y. Fu, Alloying Behavior and Novel Properties of CoCrFeNiMn High-Entropy Alloy Fabricated by Mechanical Alloying and Spark Plasma Sintering, *Intermetallics*, 2015, **56**, p 24–27.
20. Y. Liu, J.S. Wang, Q.H. Fang, B. Liu, Y. Wu, and S.Q. Chen, Preparation of Superfine-Grained High Entropy Alloy by Spark Plasma Sintering Gas Atomized Powder, *Intermetallics*, 2016, **68**, p 16–22.
21. Y. Zou, H. Ma, and R. Spolenak, Ultrastrong Ductile and Stable High-Entropy Alloys at Small Scales, *Nat. Commun.*, 2015, **6**, p 7748.
22. Y.M. Wang, T. Voisin, J.T. McKeown, J.C. Ye, N.P. Calta, Z. Li, Z. Zeng, Y. Zhang, W. Chen, T.T. Roehling, R.T. Ott, M.K. Santala, P.J. Depond, M.J. Matthews, A.V. Hamza, and T. Zhu, Additively Manufactured Hierarchical Stainless Steels with High Strength and Ductility, *Nat. Mater.*, 2018, **17**, p 63.
23. W. Chen, T. Voisin, Y. Zhang, J.-B. Florien, C. Spadaccini, D. McDowell, T. Zhu, and Y. Wang, Microscale Residual Stresses in Additively Manufactured Stainless Steel, *Nat. Commun.*, 2019, **10**, p 1–12.
24. J. Suryawanshi, K.G. Prashanth, S. Scudino, J. Eckert, O. Prakash, and U. Ramamurty, Simultaneous Enhancements of Strength and Toughness in an Al-12Si Alloy Synthesized Using Selective Laser Melting, *Acta Mater.*, 2016, **115**, p 285–294.
25. N. Raghavan, S. Simunovic, R. Dehoff, A. Plotkowski, J. Turner, M. Kirka, and S. Babu, Localized Melt-Scan Strategy for Site Specific Control of Grain Size and Primary Dendrite Arm Spacing in Electron Beam Additive Manufacturing, *Acta Mater.*, 2017, **140**, p 375–387.
26. S. Chen, Y. Tong, and P.K. Liaw, Additive Manufacturing of High-Entropy Alloys: A Review, *Entropy*, 2018, **20**, p 937.
27. M. Yan and P. Yu, An Overview of Densification, Microstructure and Mechanical Property of Additively Manufactured Ti-6Al-4V: Comparison Among Selective Laser Melting, Electron Beam Melting, Laser Metal Deposition and Selective Laser Sintering, and with Conventional Powder, 2015.
28. L. Li, Repair of Directionally Solidified Superalloy GTD-111 by Laser-Engineered Net Shaping, *J. Mater. Sci.*, 2006, **41**, p 7886–7893.
29. R. Banerjee, P.C. Collins, D. Bhattacharyya, S. Banerjee, and H.L. Fraser, Microstructural Evolution in Laser Deposited Compositionally Graded Alpha/Beta Titanium-Vanadium Alloys, *Acta Mater.*, 2003, **51**, p 3277–3292.
30. L. Jiao, Z. Chua, S. Moon, J. Song, G. Bi, and H. Zheng, Femtosecond Laser Produced Hydrophobic Hierarchical Structures on Additive Manufacturing Parts, *Nanomaterials*, 2018, **8**, p 601.
31. A.T. Sidambe, Biocompatibility of Advanced Manufactured Titanium Implants—A Review, *Materials (Basel)*, 2014, **7**, p 8168–8188.
32. S. Peng, S. Mooraj, R. Feng, L. Liu, J. Ren, Y. Liu, F. Kong, Z. Xiao, C. Zhu, P.K. Liaw, and W. Chen, Additive Manufacturing of Three-Dimensional (3D)-Architected CoCrFeNiMn High-Entropy Alloy with Great Energy Absorption, *Scr. Mater.*, 2021, **190**, p 46–51.
33. S. Mooraj, S.S. Welborn, S. Jiang, S. Peng, J. Fu, S. Baker, E.B. Duoss, C. Zhu, E. Detsi, and W. Chen, Three-Dimensional Hierarchical Nanoporous Copper Via Direct Ink Writing and Dealloying, *Scr. Mater.*, 2020, **177**, p 146–150.
34. M.L. Griffith, M.E. Schlienger, L.D. Harwell, M.S. Oliver, M.D. Baldwin, M.T. Ensz, M. Essien, J. Brooks, C.V. Robino, J.E. Smugeresky, W.H. Hofmeister, M.J. Wert, and D.V. Nelson, Understanding Thermal Behavior in the LENS Process, *Mater. Des.*, 1999, **20**, p 107–113.
35. Y. Xiong, W.H. Hofmeister, Z. Cheng, J.E. Smugeresky, E.J. Lavernia, and J.M. Schoenung, In Situ Thermal Imaging and Three-Dimensional Finite Element Modeling of Tungsten Carbide-Cobalt During Laser Deposition, *Acta Mater.*, 2009, **57**, p 5419–5429.
36. Y.H. Xiong, W.H. Hofmeister, J.E. Smugeresky, J.P. Delplanque, and J.M. Schoenung, Investigation of Atypical Molten Pool Dynamics in Tungsten Carbide-Cobalt During Laser Deposition Using In-Situ Thermal Imaging, *Appl. Phys. Lett.*, 2012, **100**, p 034101.
37. L. Wang, S.D. Felicelli, and J.E. Craig, Experimental and Numerical Study of the LENS Rapid Fabrication Process, *J. Manuf. Sci. Eng.*, 2009, **131**, p 41019.
38. S. Guan, K. Solberg, D. Wan, F. Berto, T. Welo, T.M. Yue, and K.C. Chan, Formation of Fully Equiaxed Grain Microstructure in Additively Manufactured $AlCoCrFeNiTi_{0.5}$ High Entropy Alloy, *Mater. Des.*, 2019, **184**, p 108202.
39. S. Guan, D. Wan, K. Solberg, F. Berto, T. Welo, T.M. Yue, and K.C. Chan, Additive Manufacturing of Fine-Grained and Dislocation-Populated CrMnFeCoNi High Entropy Alloy by Laser Engineered Net Shaping, *Mater. Sci. Eng. A*, 2019, **761**, p 138056.
40. S. Guan, D. Wan, K. Solberg, F. Berto, T. Welo, T.M. Yue, and K.C. Chan, Additively Manufactured CrMnFeCoNi/$AlCoCrFeNiTi_{0.5}$ Laminated High-Entropy Alloy with Enhanced Strength-Plasticity Synergy, *Scr. Mater.*, 2020, **183**, p 133–138.
41. B. Zheng, Y. Zhou, J.E. Smugeresky, J.M. Schoenung, and E.J. Lavernia, Thermal Behavior and Microstructural Evolution During Laser Deposition with Laser-Engineered Net Shaping: Part I. Numerical Calculations, *Metall. Mater. Trans. A*, 2008, **39A**, p 2228–2236.
42. L. Wang, and S. Felicelli, Analysis of Thermal Phenomena in LENS^{TM} Deposition, *Mater. Sci. Eng. A*, 2006, **435**, p 625–631.
43. L. Wang, S. Felicelli, Y. Gooroochurn, P.T. Wang, and M.F. Horstemeyer, Optimization of the LENS Process for Steady Molten Pool Size, *Mater. Sci. Eng. A*, 2008, **474**, p 148–156.
44. Y. Lu, S. Su, S. Zhang, Y. Huang, Z. Qin, X. Lu, and W. Chen, Controllable Additive Manufacturing of Gradient Bulk Metallic Glass Composite with High Strength and Tensile Ductility, *Acta Mater.*, 2021, **206**, p 116632.
45. T. DebRoy, H.L. Wei, J.S. Zuback, T. Mukherjee, J.W. Elmer, J.O. Milewski, A.M. Beese, A. Wilson-Heid, A. De, and W. Zhang, Additive Manufacturing of Metallic Components—Process, Structure and Properties, *Prog. Mater Sci.*, 2018, **92**, p 112–224.
46. T. Eagar, and N. Tsai, Temperature Fields Produced by Traveling Distributed Heat Sources, *Weld. J.*, 1983, **62**, p 346–355.
47. L. Johnson, M. Mahmoudi, B. Zhang, R. Seede, X. Huang, J.T. Maier, H.J. Maier, I. Karaman, A. Elwany, and R. Arróyave, Assessing Printability Maps in Additive Manufacturing of Metal Alloys, *Acta Mater.*, 2019, **176**, p 199–210.
48. X.Q. Wang, L.N. Carter, B. Pang, M.M. Attallah, and M.H. Loretto, Microstructure and Yield Strength of SLM-Fabricated CM247LC Ni-Superalloy, *Acta Mater.*, 2017, **128**, p 87–95.

49. R. Ye, J.E. Smugeresky, B. Zheng, Y. Zhou, and E.J. Lavernia, Numerical Modeling of the Thermal Behavior During the LENS Process, *Mater. Sci. Eng. A*, 2006, **428**, p 47–53.
50. W. Xiao, S. Li, C. Wang, Y. Shi, J. Mazumder, H. Xing, and L. Song, Multi-scale Simulation of Dendrite Growth for Direct Energy Deposition of Nickel-Based Superalloys, *Mater. Des.*, 2019, **164**, p 107553.
51. M. Moorehead, K. Bertsch, M. Niezgoda, C. Parkin, M. Elbakhshwan, K. Sridharan, C. Zhang, D. Thoma, and A. Couet, High-Throughput Synthesis of Mo-Nb-Ta-W High-Entropy Alloys Via Additive Manufacturing, *Mater. Des.*, 2020, **187**, p 108358.
52. P.P. Yuan, D.D. Gu, and D.H. Dai, Particulate Migration Behavior and Its Mechanism During Selective Laser Melting of TiC Reinforced Al Matrix Nanocomposites, *Mater. Des.*, 2015, **82**, p 46–55.
53. J.M. Park, J. Choe, J.G. Kim, J.W. Bae, J. Moon, S. Yang, K.T. Kim, J.-H. Yu, and H.S. Kim, Superior Tensile Properties of 1%C-CoCrFeMnNi High-Entropy Alloy Additively Manufactured by Selective Laser Melting, *Mater. Res. Lett.*, 2019, **8**, p 1–7.
54. P.A. Hooper, Melt Pool Temperature and Cooling Rates in Laser Powder Bed Fusion, *Addit. Manuf.*, 2018, **22**, p 548–559.
55. M. Gäumann, S. Henry, F. Cleton, J.D. Wagniere, and W. Kurz, Epitaxial Laser Metal Forming: Analysis of Microstructure Formation, *Mater. Sci. Eng. A*, 1999, **271**, p 232–241.
56. G.P. Dinda, A.K. Dasgupta, and J. Mazumder, Laser Aided Direct Metal Deposition of Inconel 625 Superalloy: Microstructural Evolution and Thermal Stability, *Mater. Sci. Eng. A*, 2009, **509**, p 98–104.
57. Y. Kok, X.P. Tan, P. Wang, M.L.S. Nai, N.H. Loh, E. Liu, and S.B. Tor, Anisotropy and Heterogeneity of Microstructure and Mechanical Properties in Metal Additive Manufacturing: A Critical Review, *Mater. Des.*, 2018, **139**, p 565–586.
58. P. Hou, Y. Li, D. Chae, Y. Ren, K. An, and H. Choo, Lean Duplex TRIP Steel: Role of Ferrite in the Texture Development, Plastic Anisotropy, Martensitic Transformation Kinetics, and Stress Partitioning, *Materialia*, 2021, **15**, p 100952.
59. X. Lin, T.M. Yue, H.O. Yang, and W.D. Huang, Microstructure and Phase Evolution in Laser Rapid Forming of a Functionally Graded Ti-Rene88DT Alloy, *Acta Mater.*, 2006, **54**, p 1901–1915.
60. X. Lin, T.M. Yue, H.O. Yang, and W.D. Huang, Laser Rapid Forming of SS316L/Rene88DT Graded Material, *Mater. Sci. Eng. A*, 2005, **391**, p 325–336.
61. X. Lin, and T.M. Yue, Phase Formation and Microstructure Evolution in Laser Rapid Forming of Graded SS316L/Rene88DT Alloy, *Mater. Sci. Eng. A*, 2005, **402**, p 294–306.
62. Y.M. Li, H. Yang, X. Lin, W.D. Huang, J.G. Li, and Y.H. Zhou, The Influences of Processing Parameters on Forming Characterizations During Laser Rapid Forming, *Mater. Sci. Eng. A*, 2003, **360**, p 18–25.
63. W. Kurz, C. Bezencon, and M. Gäumann, Columnar to Equiaxed Transition in Solidification Processing, *Sci. Technol. Adv. Mat.*, 2001, **2**, p 185–191.
64. M. Gäumann, C. Bezencon, P. Canalis, and W. Kurz, Single-Crystal Laser Deposition of Superalloys: Processing-Microstructure Maps, *Acta Mater.*, 2001, **49**, p 1051–1062.
65. D. Dube, M. Fiset, A. Couture, and I. Nakatsugawa, Characterization and Performance of Laser Melted AZ91D and AM60B, *Mater. Sci. Eng. A*, 2001, **299**, p 38–45.
66. F. Cleton, P.H. Jouneau, S. Henry, M. Gaumann, and P.A. Buffat, Crystallographic Orientation Assessment by Electron Backscattered Diffraction, *Scanning*, 1999, **21**, p 232–237.
67. R. Banerjee, P.C. Collins, A. Genc, and H.L. Fraser, Direct Laser Deposition of In Situ Ti-6Al-4V-TiB Composites, *Mater. Sci. Eng. A*, 2003, **358**, p 343–349.
68. R.S. Amano, and P.K. Rohatgi, Laser Engineered Net Shaping Process for SAE 4140 Low Alloy Steel, *Mater. Sci. Eng. A*, 2011, **528**, p 6680–6693.
69. R. Banerjee, C.A. Brice, S. Banerjee, and H.L. Fraser, Microstructural Evolution in Laser Deposited Ni-25at.% Mo Alloy, *Mater. Sci. Eng. A*, 2003, **347**, p 1–4.
70. Y.Y. Zhu, D. Liu, X.J. Tian, H.B. Tang, and H.M. Wang, Characterization of Microstructure and Mechanical Properties of Laser Melting Deposited Ti-6.5Al-3.5Mo-1.5Zr-0.3Si Titanium Alloy, *Mater. Des.*, 2014, **56**, p 445–453.
71. L.L. Parimi, G.A. Ravi, D. Clark, and M.M. Attallah, Microstructural and Texture Development in Direct Laser Fabricated IN718, *Mater. Charact.*, 2014, **89**, p 102–111.
72. I. Kunce, M. Polanski, K. Karczewski, T. Plocinski, and K.J. Kurzydlowski, Microstructural Characterisation of High-Entropy Alloy AlCoCrFeNi Fabricated by Laser Engineered Net Shaping, *J. Alloys Compd.*, 2015, **648**, p 751–758.
73. M. Gäumann, R. Trivedi, and W. Kurz, Nucleation Ahead of the Advancing Interface in Directional Solidification, *Mater. Sci. Eng. A*, 1997, **226**, p 763–769.
74. J.D. Hunt, Steady-State Columnar and Equiaxed Growth of Dendrites and Eutectic, *Mater. Sci. Eng.*, 1984, **65**, p 75–83.
75. Y.B. Zuo, B. Jiang, Y. Zhang, and Z. Fan, Iop, Grain Refinement of DC Cast Magnesium Alloys with Intensive Melt Shearing, in *3rd International Conference on Advances in Solidification Processes* (2012).
76. Y.H. Zhang, X.R. Cheng, H.G. Zhong, Z.S. Xu, L.J. Li, Y.Y. Gong, X.C. Miao, C.J. Song, and Q.J. Zhai, Comparative Study on the Grain Refinement of Al-Si Alloy Solidified Under the Impact of Pulsed Electric Current and Travelling Magnetic Field, *Metals*, 2016, **6**, p 170.
77. T. Yuan, Z. Luo, and S. Kou, Grain Refining of Magnesium welds by Arc Oscillation, *Acta Mater.*, 2016, **116**, p 166–176.
78. C.J. Todaro, M.A. Easton, D. Qiu, D. Zhang, M.J. Bermingham, E.W. Lui, M. Brandt, D.H. StJohn, and M. Qian, Grain Structure Control During Metal 3D Printing by High-Intensity Ultrasound, *Nat. Commun.*, 2020, **11**, p 142.
79. T. Fujieda, H. Shiratori, K. Kuwabara, T. Kato, K. Yamanaka, Y. Koizumi, and A. Chiba, First Demonstration of Promising Selective Electron Beam Melting Method for Utilizing High-Entropy Alloys as Engineering Materials, *Mater. Lett.*, 2015, **159**, p 12–15.
80. P. Kürnsteiner, M.B. Wilms, A. Weisheit, B. Gault, E.A. Jägle, and D. Raabe, High-Strength Damascus Steel by Additive Manufacturing, *Nature*, 2020, **582**, p 515–519.
81. Z.G. Zhu, Q.B. Nguyen, F.L. Ng, X.H. An, X.Z. Liao, P.K. Liaw, S.M.L. Nai, and J. Wei, Hierarchical Microstructure and Strengthening Mechanisms of a CoCrFeNiMn High Entropy Alloy Additively Manufactured by Selective Laser Melting, *Scr. Mater.*, 2018, **154**, p 20–24.
82. R.D. Li, P.D. Niu, T.C. Yuan, P. Cao, C. Chen, and K.C. Zhou, Selective Laser Melting of an Equiatomic CoCrFeMnNi High-Entropy Alloy: Processability, Non-equilibrium Microstructure and Mechanical Property, *J. Alloys Compd.*, 2018, **746**, p 125–134.

83. A. Piglione, B. Dovgyy, C. Liu, C.M. Gourlay, P.A. Hooper, and M.S. Pham, Printability and Microstructure of the CoCrFeMnNi High-Entropy Alloy Fabricated by Laser Powder Bed Fusion, *Mater. Lett.*, 2018, **224**, p 22–25.
84. Z. Qiu, C. Yao, K. Feng, Z. Li, and P.K. Chu, Cryogenic Deformation Mechanism of CrMnFeCoNi High-Entropy Alloy Fabricated by Laser Additive Manufacturing Process, *Int. J. Lightweight Mater. Manuf.*, 2018, **1**, p 33–39.
85. S. Xiang, H.W. Luan, J. Wu, K.F. Yao, J.F. Li, X. Liu, Y.Z. Tian, W.L. Mao, H. Bai, G.M. Le, and Q. Li, Microstructures and Mechanical Properties of CrMnFeCoNi High Entropy Alloys Fabricated Using Laser Metal Deposition Technique, *J. Alloys Compd.*, 2019, **773**, p 387–392.
86. X. Gao, and Y. Lu, Laser 3D Printing of CoCrFeMnNi High-Entropy Alloy, *Mater. Lett.*, 2019, **236**, p 77–80.
87. Z. Tong, X. Ren, J. Jiao, W. Zhou, Y. Ren, Y. Ye, E.A. Larson, and J. Gu, Laser Additive Manufacturing of FeCrCoMnNi High-Entropy Alloy: Effect of Heat Treatment on Microstructure, Residual Stress and Mechanical Property, *J. Alloys Compd.*, 2019, **785**, p 1144–1159.
88. Y. Chew, G.J. Bi, Z.G. Zhu, F.L. Ng, F. Weng, S.B. Liu, S.M.L. Nai, and B.Y. Lee, Microstructure and Enhanced Strength of Laser Aided Additive Manufactured CoCrFeNiMn High Entropy Alloy, *Mater. Sci. Eng. A*, 2019, **744**, p 137–144.
89. M.A. Melia, J.D. Carroll, S.R. Whetten, S.N. Esmaeely, J. Locke, E. White, I. Anderson, M. Chandross, J.R. Michael, N. Argibay, E.J. Schindelholz, and A.B. Kustas, Mechanical and Corrosion Properties of Additively Manufactured CoCrFeMnNi High Entropy Alloy, *Addit. Manuf.*, 2019, **29**, p 100833.
90. W. Zhao, J.-K. Han, Y.O. Kuzminova, S.A. Evlashin, A.P. Zhilyaev, A.M. Pesin, J.-I. Jang, K.-D. Liss, and M. Kawasaki, Significance of Grain Refinement on Micro-Mechanical Properties and Structures of Additively-Manufactured CoCrFeNi High-Entropy Alloy, *Mater. Sci. Eng. A*, 2021, **807**, p 140898.
91. J. Ren, C. Mahajan, L. Liu, D. Follette, W. Chen, and S. Mukherjee, Corrosion behavior of Selectively Laser Melted CoCrFeMnNi High Entropy Alloy, *Metals*, 2019, **9**, p 1029.
92. H. Shiratori, T. Fujieda, K. Yamanaka, Y. Koizumi, K. Kuwabara, T. Kato, and A. Chiba, Relationship Between the Microstructure and Mechanical Properties of an Equiatomic AlCoCrFeNi High-Entropy Alloy Fabricated by Selective Electron Beam Melting, *Mater. Sci. Eng. A*, 2016, **656**, p 39–46.
93. J. Joseph, P. Hodgson, T. Jarvis, X.H. Wu, N. Stanford, and D.M. Fabijanic, Effect of Hot Isostatic Pressing on the Microstructure and Mechanical Properties of Additive Manufactured Al_xCoCrFeNi High Entropy Alloys, *Mater. Sci. Eng. A*, 2018, **733**, p 59–70.
94. J. Joseph, T. Jarvis, X.H. Wu, N. Stanford, P. Hodgson, and D.M. Fabijanic, Comparative Study of the Microstructures and Mechanical Properties of Direct Laser Fabricated and Arc-Melted Al_xCoCrFeNi High Entropy Alloys, *Mater. Sci. Eng. A*, 2015, **633**, p 184–193.
95. J. Joseph, N. Stanford, P. Hodgson, and D.M. Fabijanic, Tension/Compression Asymmetry in Additive Manufactured Face Centered Cubic High Entropy Alloy, *Scr. Mater.*, 2017, **129**, p 30–34.
96. Z. Sun, X.P. Tan, M. Descoins, D. Mangelinck, S.B. Tor, and C.S. Lim, Revealing Hot Tearing Mechanism for an Additively Manufactured High-Entropy Alloy Via Selective Laser Melting, *Scr. Mater.*, 2019, **168**, p 129–133.
97. Y. Brif, M. Thomas, and I. Todd, The Use of High-Entropy Alloys in Additive Manufacturing, *Scr. Mater.*, 2015, **99**, p 93–96.
98. R. Zhou, Y. Liu, C.S. Zhou, S.Q. Li, W.Q. Wu, M. Song, B. Liu, X.P. Liang, and P.K. Liaw, Microstructures and Mechanical Properties of C-Containing FeCoCrNi High-Entropy Alloy Fabricated by Selective Laser Melting, *Intermetallics*, 2018, **94**, p 165–171.
99. D. Choudhuri, T. Alam, T. Borkar, B. Gwalani, A.S. Mantri, S.G. Srinivasan, M.A. Gibson, and R. Banerjee, Formation of a Huesler-Like $L2_1$ Phase in a CoCrCuFeNiAlTi High-Entropy Alloy, *Scr. Mater.*, 2015, **100**, p 36–39.
100. I. Kunce, M. Polanski, and J. Bystrzycki, Microstructure and Hydrogen Storage Properties of a TiZrNbMoV High Entropy Alloy Synthesized Using Laser Engineered Net Shaping (LENS), *Int. J. Hydrogen Energy*, 2014, **39**, p 9904–9910.
101. T. Fujieda, H. Shiratori, K. Kuwabara, M. Hirota, T. Kato, K. Yamanaka, Y. Koizumi, A. Chiba, and S. Watanabe, CoCrFeNiTi-Based High-Entropy Alloy with Superior Tensile Strength and Corrosion Resistance Achieved by a Combination of Additive Manufacturing Using Selective Electron Beam Melting and Solution Treatment, *Mater. Lett.*, 2017, **189**, p 148–151.
102. P.K. Sarswat, S. Sarkar, A. Murali, W. Huang, W. Tan, and M.L. Free, Additive Manufactured New Hybrid High Entropy Alloys Derived from the AlCoFeNiSmTiVZr System, *Appl. Surf. Sci.*, 2019, **476**, p 242–258.
103. T. Borkar, V. Chaudhary, B. Gwalani, D. Choudhuri, C.V. Mikler, V. Soni, T. Alam, R.V. Ramanujan, and R. Banerjee, A Combinatorial Approach for Assessing the Magnetic Properties of High Entropy Alloys: Role of Cr in $AlCo_xCr_{1-x}FeNi$, *Adv. Eng. Mater.*, 2017, **19**, p 1700048.
104. T. Borkar, B. Gwalani, D. Choudhuri, C.V. Mikler, C.J. Yannetta, X. Chen, R.V. Ramanujan, M.J. Styles, M.A. Gibson, and R. Banerjee, A Combinatorial Assessment of $Al_xCrCuFeNi_2$ ($0 < x < 1.5$) Complex Concentrated Alloys: Microstructure, Microhardness, and Magnetic Properties, *Acta Mater.*, 2016, **116**, p 63–76.
105. B. Gwalani, V. Soni, O.A. Waseem, S.A. Mantri, and R. Banerjee, Laser Additive Manufacturing of Compositionally Graded $AlCrFeMoV_x$ (x = 0 to 1) High-Entropy Alloy System, *Opt. Laser Technol.*, 2019, **113**, p 330–337.
106. H. Dobbelstein, E.L. Gurevich, E.P. George, A. Ostendorf, and G. Laplanche, Laser Metal Deposition Of Compositionally Graded TiZrNbTa Refractory High-Entropy Alloys Using Elemental Powder Blends, *Addit. Manuf.*, 2019, **25**, p 252–262.
107. Y. Cai, L. Zhu, Y. Cui, and J. Han, Manufacturing of FeCoCrNi + FeCoCrNiAl Laminated High-Entropy Alloy by Laser Melting Deposition (LMD), *Mater. Lett.*, 2021, **289**, p 129445.
108. Y.-K. Kim, J. Choe, and K.-A. Lee, Selective Laser Melted Equiatomic CoCrFeMnNi High-Entropy Alloy: Microstructure, Anisotropic Mechanical Response, and Multiple Strengthening Mechanism, *J. Alloys Compd.*, 2019, **805**, p 680–691.
109. H. Li, Y. Huang, S. Jiang, Y. Lu, X. Gao, X. Lu, Z. Ning, and J. Sun, Columnar to Equiaxed Transition in Additively Manufactured CoCrFeMnNi High Entropy Alloy, *Mater. Des.*, 2020, **197**, p 109262.
110. M. Zheng, C. Li, X. Zhang, Z. Ye, X. Yang, and J. Gu, The Influence of Columnar to Equiaxed Transition on Deformation Behavior of FeCoCrNiMn High Entropy Alloy Fabricated by Laser-Based Directed Energy Deposition, *Addit. Manuf.*, 2020, **37**, p 101660.
111. C. Haase, F. Tang, M.B. Wilms, A. Weisheit, and B. Hallstedt, Combining Thermodynamic Modeling and 3D Printing of Elemental Powder Blends for High-Throughput Investigation of High-Entropy Alloys—Towards Rapid Alloy Screening and Design, *Mater. Sci. Eng. A*, 2017, **688**, p 180–189.

112. L. Liu, Q. Ding, Y. Zhong, J. Zou, J. Wu, Y.-L. Chiu, J. Li, Z. Zhang, Q. Yu, and Z. Shen, Dislocation Network in Additive Manufactured Steel Breaks Strength-Ductility Trade-Off, *Mater. Today*, 2018, **21**, p 354–361.
113. J. Chen, Z. Yao, X. Wang, Y. Lu, X. Wang, Y. Liu, and X. Fan, Effect of C Content on Microstructure and Tensile Properties of As-Cast CoCrFeMnNi High Entropy Alloy, *Mater. Chem. Phys.*, 2018, **210**, p 136–145.
114. F. Otto, A. Dlouhy, C. Somsen, H. Bei, G. Eggeler, and E.P. George, The Influences of Temperature and Microstructure on the Tensile Properties of a CoCrFeMnNi High-Entropy Alloy, *Acta Mater.*, 2013, **61**, p 5743–5755.
115. S.J. Sun, Y.Z. Tian, H.R. Lin, X.G. Dong, Y.H. Wang, Z.J. Zhang, and Z.F. Zhang, Enhanced Strength and Ductility of Bulk CoCrFeMnNi High Entropy Alloy Having Fully Recrystallized Ultrafine-Grained Structure, *Mater. Des.*, 2017, **133**, p 122–127.
116. H. Shahmir, J. He, Z. Lu, M. Kawasaki, and T.G. Langdon, Effect of Annealing on Mechanical Properties of a Nanocrystalline CoCrFeNiMn High-Entropy Alloy Processed by High-Pressure Torsion, *Mater. Sci. Eng. A*, 2016, **676**, p 294–303.
117. C. Kenel, N.P.M. Casati, and D.C. Dunand, 3D Ink-Extrusion Additive Manufacturing of CoCrFeNi High-Entropy Alloy Micro-lattices, *Nat. Commun.*, 2019, **10**, p 904.
118. Y.-K. Kim, M.-S. Baek, S. Yang, and K.-A. Lee, In-Situ Formed Oxide Enables Extraordinary High-Cycle Fatigue Resistance in Additively Manufactured CoCrFeMnNi High-Entropy Alloy, *Addit. Manuf.*, 2021, **38**, p 101832.
119. R. Zhou, Y. Liu, B. Liu, J. Li, and Q. Fang, Precipitation Behavior of Selective Laser Melted $FeCoCrNiC_{0.05}$ High Entropy Alloy, *Intermetallics*, 2019, **106**, p 20–25.
120. B. Li, L. Zhang, and B. Yang, Grain Refinement and Localized Amorphization of Additively Manufactured High-Entropy Alloy Matrix Composites Reinforced by Nano Ceramic Particles Via Selective-Laser-Melting/Remelting, *Compos. Commun.*, 2020, **19**, p 56–60.
121. B. Li, L. Zhang, Y. Xu, Z. Liu, B. Qian, and F. Xuan, Selective Laser Melting of CoCrFeNiMn High Entropy Alloy Powder Modified with Nano-TiN Particles for Additive Manufacturing and Strength Enhancement: Process, Particle Behavior and Effects, *Powder Technol.*, 2020, **360**, p 509–521.
122. B. Li, B. Qian, Y. Xu, Z. Liu, and F. Xuan, Fine-Structured CoCrFeNiMn High-Entropy Alloy Matrix Composite with 12 wt% TiN Particle Reinforcements Via Selective Laser Melting Assisted Additive Manufacturing, *Mater. Lett.*, 2019, **252**, p 88–91.
123. J. Li, S. Xiang, H. Luan, A. Amar, X. Liu, S. Lu, Y. Zeng, G. Le, X. Wang, F. Qu, C. Jiang, and G. Yang, Additive Manufacturing of High-Strength CrMnFeCoNi High-Entropy Alloys-Based Composites with WC Addition, *J. Mater. Sci. Technol.*, 2019, **35**, p 2430–2434.
124. A. Amar, J. Li, S. Xiang, X. Liu, Y. Zhou, G. Le, X. Wang, F. Qu, S. Ma, W. Dong, and Q. Li, Additive Manufacturing of High-Strength CrMnFeCoNi-Based High Entropy Alloys with TiC Addition, *Intermetallics*, 2019, **109**, p 162–166.
125. X. Gao, Z. Yu, W. Hu, Y. Lu, Z. Zhu, Y. Ji, Y. Lu, Z. Qin, and X. Lu, In Situ Strengthening of CrMnFeCoNi High-Entropy Alloy with Al Realized by Laser Additive Manufacturing, *J. Alloys Compd.*, 2020, **847**, p 156563.
126. M.S.K.K.Y. Nartu, T. Alam, S. Dasari, S.A. Mantri, S. Gorsse, H. Siller, N. Dahotre, and R. Banerjee, Enhanced Tensile Yield Strength in Laser Additively Manufactured $Al_{0.3}CoCrFeNi$ High Entropy Alloy, *Materialia*, 2020, **9**, p 100522.
127. K. Zhou, Z. Wang, F. He, S. Liu, J. Li, J.-J. Kai, and J. Wang, A Precipitation-Strengthened high-Entropy Alloy for Additive Manufacturing, *Addit. Manuf.*, 2020, **35**, p 101410.
128. W.-C. Lin, Y.-J. Chang, T.-H. Hsu, S. Gorsse, F. Sun, T. Furuhara, and A.-C. Yeh, Microstructure and Tensile Property of a Precipitation Strengthened High Entropy Alloy Processed by Selective Laser Melting and Post Heat Treatment, *Addit. Manuf.*, 2020, **36**, p 101601.
129. I. Kunce, M. Polanski, and J. Bystrzycki, Structure and Hydrogen Storage Properties of a High Entropy ZrTiVCrFeNi Alloy Synthesized Using Laser Engineered Net Shaping (LENS), *Int. J. Hydrogen Energy*, 2013, **38**, p 12180–12189.
130. H. Zhang, Y. Zhao, J. Cai, S. Ji, J. Geng, X. Sun, and D. Li, High-Strength NbMoTaX Refractory High-Entropy Alloy with Low Stacking Fault Energy Eutectic Phase Via Laser Additive Manufacturing, *Mater. Des.*, 2021, **201**, p 109462.
131. Z. Li, K.G. Pradeep, Y. Deng, D. Raabe, and C.C. Tasan, Metastable High-Entropy Dual-Phase Alloys Overcome the Strength-Ductility Trade-Off, *Nature*, 2016, **534**, p 227.
132. P. Agrawal, S. Thapliyal, S.S. Nene, R.S. Mishra, B.A. McWilliams, and K.C. Cho, Excellent Strength-Ductility Synergy in Metastable High Entropy Alloy by Laser Powder Bed Additive Manufacturing, *Addit. Manuf.*, 2020, **32**, p 101098.
133. S. Thapliyal, S.S. Nene, P. Agrawal, T. Wang, C. Morphew, R.S. Mishra, B.A. McWilliams, and K.C. Cho, Damage-Tolerant, Corrosion-Resistant High Entropy Alloy with High Strength and Ductility by Laser Powder Bed Fusion Additive Manufacturing, *Addit. Manuf.*, 2020, **36**, p 101455.
134. B. Gwalani, S. Gangireddy, S. Shukla, C.J. Yannetta, S.G. Valentin, R.S. Mishra, and R. Banerjee, Compositionally Graded High Entropy Alloy with a Strong Front and Ductile Back, *Mater. Today Commun.*, 2019, **20**, p 100602.
135. J.W. Pegues, M.A. Melia, R. Puckett, S.R. Whetten, N. Argibay, and A.B. Kustas, Exploring Additive Manufacturing as a High-Throughput Screening Tool for Multiphase High Entropy Alloys, *Addit. Manuf.*, 2021, **37**, p 101598.
136. Y. Li, Q. Zhou, S. Zhang, P. Huang, K. Xu, F. Wang, and T. Lu, On the Role of Weak Interface in Crack Blunting Process in Nanoscale Layered Composites, *Appl. Surf. Sci.*, 2018, **433**, p 957–962.
137. A. Rohatgi, D.J. Harach, K.S. Vecchio, and K.P. Harvey, Resistance-Curve and Fracture Behavior of Ti-Al_3Ti Metallic-Intermetallic Laminate (MIL) Composites, *Acta Mater.*, 2003, **51**, p 2933–2957.
138. J.G. Kim, J.M. Park, J.B. Seol, J. Choe, J.H. Yu, S. Yang, and H.S. Kim, Nano-scale Solute Heterogeneities in the Ultrastrong Selectively Laser Melted Carbon-Doped CoCrFeMnNi Alloy, *Mater. Sci. Eng. A*, 2020, **773**, p 9.
139. V.V. Popov, A. Katz-Demyanetz, A. Koptyug, and M. Bamberger, Selective Electron Beam Melting of $Al_{0.5}CrMoNbTa_{0.5}$ High Entropy Alloys Using Elemental Powder Blend, *Heliyon*, 2019, **5**, p e01188.
140. S.H. Joo, H. Kato, M.J. Jang, J. Moon, E.B. Kim, S.J. Hong, and H.S. Kim, Structure and Properties of Ultrafine-Grained CoCrFeMnNi High-Entropy Alloys Produced by Mechanical Alloying and Spark Plasma Sintering, *J. Alloys Compd.*, 2017, **698**, p 591–604.
141. Y.H. Zhou, Z.H. Zhang, Y.P. Wang, G. Liu, S.Y. Zhou, Y.L. Li, J. Shen, and M. Yan, Selective Laser Melting of Typical Metallic Materials: An Effective Process Prediction Model Developed by Energy Absorption and Consumption Analysis, *Addit. Manuf.*, 2019, **25**, p 204–217.
142. Y. Kuzminova, D. Firsov, A. Dudin, S. Sergeev, A. Zhilyaev, A. Dyakov, A. Chupeeva, A. Alekseev, D. Martynov, I. Akhatov, and S. Evlashin, The Effect of the Parameters Of The Powder Bed Fusion Process on the Microstructure and Mechanical Properties of CrFeCoNi Medium-Entropy Alloys, *Intermetallics*, 2020, **116**, p 106651.

143. Z. Wang, J. Gu, D. An, Y. Liu, and M. Song, Characterization of the Microstructure and Deformation Substructure Evolution in a Hierarchal High-Entropy Alloy by Correlative EBSD and ECCI, *Intermetallics*, 2020, **121**, p 106788.
144. M. Song, R. Zhou, J. Gu, Z. Wang, S. Ni, and Y. Liu, Nitrogen Induced Heterogeneous Structures Overcome Strength-Ductility Trade-Off in an Additively Manufactured High-Entropy Alloy, *Appl. Mater. Today*, 2020, **18**, p 100498.
145. X. Yang, Y. Zhou, S. Xi, Z. Chen, P. Wei, C. He, T. Li, Y. Gao, and H. Wu, Additively Manufactured Fine Grained $Ni_6Cr_4WFe_9Ti$ High Entropy Alloys with High Strength and Ductility, *Mater. Sci. Eng. A*, 2019, **767**, p 138394.
146. X. Yang, Y. Zhou, S. Xi, Z. Chen, P. Wei, C. He, T. Li, Y. Gao, and H. Wu, Grain-Anisotropied High-Strength $Ni_6Cr_4WFe_9Ti$ High Entropy Alloys with Outstanding Tensile Ductility, *Mater. Sci. Eng. A*, 2019, **767**, p 138382.
147. T. Fujieda, M. Chen, H. Shiratori, K. Kuwabara, K. Yamanaka, Y. Koizumi, A. Chiba, and S. Watanabe, Mechanical and Corrosion Properties of CoCrFeNiTi-Based High-Entropy Alloy Additive Manufactured Using Selective Laser Melting, *Addit. Manuf.*, 2019, **25**, p 412–420.